Femtochemistry of Norrish Type-I Reactions: I. Experimental and Theoretical Studies of Acetone and Related Ketones on the S_1 Surface

Eric W.-G. Diau, Carsten Kötting, and Ahmed H. Zewail*[a]

The dissociation dynamics of two acetone isotopomers ([D_0]- and [D_6]acetone) after 93 kcal mol^{-1} (307 nm) excitation to the $S_1(n,\pi^*)$ state have been investigated using femtosecond pump–probe mass spectrometry. We found that the nuclear motions of the molecule on the S_1 surface involve two time scales. The initial femtosecond motion corresponds to the dephasing of the wave packet out of the Franck–Condon region on the S_1 surface. For longer times, the direct observation of the build-up of the acetyl radical confirms that the S_1 α-cleavage dynamics of acetone is on the nanosecond time scale. Density functional theory and ab initio calculations have been carried out to characterize the potential energy surfaces for the S_0, S_1, and T_1 states of acetone and six other related aliphatic ketones. For acetone, the S_1 energy barrier along the single α-positioned carbon–carbon (α-CC) bond-dissociation coordinate (to reach the S_0/S_1 conical intersection) was calculated to be 18 kcal mol^{-1} (~ 110 kcal mol^{-1} above the S_0 minimum) for the first step of the nonconcerted α-CC bond cleavage; the concerted path is energetically unfavorable, consistent with experiments. The S_1 barrier heights for other aliphatic ketones were found to be substantially lower than that of acetone by methyl substitutions at the α-position. The α-CC bond dissociation energy barrier of acetone on the T_1 surface was calculated to be only 5 kcal mol^{-1} (~ 90 kcal mol^{-1} above the S_0 minimum), which is substantially lower than the barrier on the S_1 surface. Based on the calculations, the α-cleavage reaction mechanism of acetone occurring on the S_0, S_1, and T_1 surfaces can be better understood via a simple physical picture within the framework of valence-bond theory. The theoretical calculations support the conclusion that the observed nanosecond-scale S_1 dynamics of acetone below the barrier is governed by a rate-limiting $S_1 \rightarrow T_1$ intersystem crossing process followed by α-cleavage on the T_1 surface. However, at high energies, the α-cleavage can proceed by barrier crossing on the S_1 surface, a situation which is demonstrated for cyclobutanone in the accompanying paper.

KEYWORDS:

acetone · conical intersections · femtochemistry · mass spectrometry · Norrish reactions

1. Introduction

Photoexcitation of an aliphatic ketone from the ground state (S_0) to its first electronically excited singlet state (S_1) leads primarily to the cleavage of one of the α-CC bonds (α-cleavage). The products are an acyl radical and an alkyl radical. This fundamental photochemical process is known as Norrish type-I reaction.[1] The detailed α-cleavage reaction mechanism and the related dynamic behavior are the key to understanding the photochemistry for the entire family of carbonyl compounds.[2–5] A classic example is the photodissociation of acetone, which has been the subject of numerous intensive investigations over many decades (see refs. [6–28], and references therein).
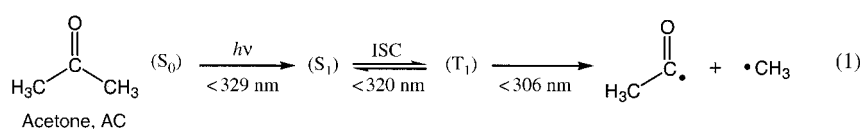
The $S_0 \rightarrow S_1$ transition of acetone involves a perpendicular electronic excitation from the nonbonding n orbital of the oxygen atom to the antibonding π^* orbital. This dipole-forbidden n $\rightarrow \pi^*$ transition ($\tilde{A}^1A_2 \leftarrow \tilde{X}^1A_1$) is characterized by a weak and broad absorption band from 330 to 220 nm with its maximum around 280 nm;[29] the intensity is "borrowed" from higher-lying symmetry-allowed transitions through vibronic coupling. This intensity-borrowing mechanism, originally conceived by Herzberg and Teller,[30] has been supported by calculations of the vibronic spectra of acetone using high-level ab initio methods[31] and analysis of the experimental fluorescence excitation spectra performed on isolated acetone.[32]

The initial photophysical transformation of acetone near the onset of the $S_0 \rightarrow S_1$ excitation ($\lambda_{ex} \sim 329$ nm) has been proposed to result in the emission of fluorescence via the $S_1 \rightarrow S_0$ transition, undergo intersystem crossing (ISC) to the lowest triplet state (T_1), and internally convert to the hot ground state (S_0^*).[12, 29, 33, 34] Since the fluorescence quantum yield (Φ_F) is only ~ 0.002,[35] the primary S_1 relaxation is dominated by nonradiative processes. For example, at the 0-0 band origin ($\lambda_{ex} = 328.6$ nm), the fluorescence lifetime (τ_s) of an isolated acetone was observed to be ~ 1 μs, presumably due to the $S_1 \rightarrow S_0$ internal conversion (IC) process.[34] However, with the excess energy more than

[a] Prof. A. H. Zewail, Dr. E. W.-G. Diau, Dr. C. Kötting
Arthur Amos Noyes Laboratory of Chemical Physics
California Institute of Technology
Pasadena, CA 91125 (USA)
Fax: (+ 1)626-792-8456
E-mail: zewail@caltech.edu

$\sim 900\,\mathrm{cm}^{-1}$ above the S_1 origin ($\lambda_{ex} < 320$ nm), the $S_1 \rightarrow T_1$ ISC process was observed on the nanosecond (ns) time scale.[34] The dissociation threshold of acetone has been reported to be at $\lambda_{ex} = 305.8$ nm, where the microsecond-decay component was suddenly diminished.[34] The fluorescence lifetime of acetone was also determined in gas-phase bulk experiments to be 2.7 ns at $\lambda_{ex} = 313$ nm and decreasing smoothly down to < 1.6 ns at $\lambda_{ex} = 260$ nm.[29, 33] The observed ns lifetimes of the S_1 acetone at the excitation above its dissociation threshold is consistent with the isotropic spatial distribution of the fragments measured by the ns-scaled photofragmentation translational spectroscopy at $\lambda_{ex} = 266$[36] and 248 nm.[20] According to the experimental findings mentioned above,[32–34] the dissociation of acetone upon excitation to the $S_1(n,\pi^*)$ state is proposed to proceed over an energy barrier on the T_1 surface after the $S_1 \rightarrow T_1$ ISC process, Equation (1).

Figure 1. State-correlation diagram of acetone along the single α-CC bond-breaking reaction coordinate to form either a bent (right) or a linear (left) acetyl radical. The dashed lines represent symmetry-adapted state correlations (S: symmetrical; A: antisymmetrical) of different electronic configurations with respect to the molecular symmetry plane of the carbon skeleton. The ground state is marked GS.

This S_1 photodissociation mechanism of acetone has been challenged by recent femtosecond (fs) real-time observations. According to these fs pump–probe studies,[22, 24, 26] two common features were reported for the observed ion signals for λ_{ex} in the range 253 – 268 nm. First, all the fs studies showed that the parent transient involves a dominating pulse-limited fast-decay component with a time constant less than 200 fs. Second, the fragment transient corresponding to the acetyl mass has two components; the fast-decay component is similar to that of the parent ion signal whereas the "offset" component persists on the picosecond (ps) time scale. On one hand, photofragment ion image measurement[22] has shown the isotropic distribution of the acetyl ion from 1 to 15 ps, suggesting that the observed offset component in the acetyl ion signal is due to fragmentation of the parent ion. This has led to the conclusion that the S_1 acetone is long-lived at $\lambda_{ex} = 253$ nm, which is consistent with the ns-scale lifetimes[33] earlier reported and the observed isotropic product distribution[20, 36] in the similar wavelength region. On the other hand, the persistent offset component was not detectable in the parent transient, to lead to a totally reversed conclusion: The primary α-CC bond breakage of acetone is prompt (< 200 fs).[24, 26] Such ultrafast bond-breaking mechanism for the Norrish type-I reaction of acetone in the S_1 state contradicts the commonly accepted mechanism and certainly deserves further experimental and theoretical investigations.

Based on the assumption of the state-correlation diagram and the results of early ab initio calculations,[6] the picture for the photochemistry of Norrish type-I reactions was proposed more than two decades ago. The state-correlation diagram of singlet acetone is shown in Figure 1, where the dashed lines represent
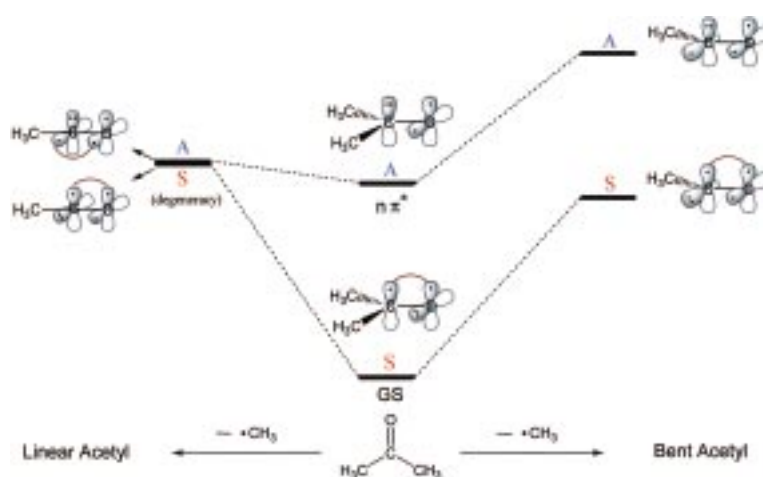
the symmetry-adapted state correlations of different electronic configurations with respect to the molecular symmetry plane for both bent and linear reaction pathways.[3]

Based on a zeroth-order approach, this correlation diagram states that the α-cleavage of the $S_1(n,\pi^*)$ ketones to produce a bent acyl fragment (such as an acetyl radical from acetone) is symmetry-forbidden whereas the formation of a linear acyl fragment is symmetry-allowed.[37] In other words, the excited ketone molecule will initially relax to a geometry with the linear acyl fragment configuration on the $S_1(n,\pi^*)$ surface, in which the S_1 and the S_0 states are degenerate.[6] However, as pointed out by Salem,[6] the state-correlation diagram only provides a qualitative theoretical description for the Norrish type-I reaction mechanism because the symmetry of the molecular plane may not be always retained along the α-cleavage reaction coordinate (RC) on the excited-state potential energy surfaces (PESs).

Recently, high-level ab initio calculations[8–11] based on multi-reference (MR) wave functions were carried out to characterize the S_1 and T_1 PESs along the single α-CC bond-breaking RC. Following the single α-CC bond-dissociation pathway, the transition states (TS) on both S_1 and T_1 surfaces were shown to have the CC bond distance (RC) in the range of 1.9 – 2.1 Å.[8–11] The energy barrier of the T_1-TS calculated at the MR Møller–Plesset (MP) levels[8b, 9] is comparable with the experimental threshold value (93.5 kcal mol^{-1} above the S_0 minimum),[34d] whereas that of the S_1-TS predicted at the complete active space self-consistent field (CASSCF) level[11] lies as high as 133 kcal mol^{-1} above the S_0 minimum. The statistical α-cleavage reaction rate on the T_1 surface was calculated using Rice-Ramsperger-Kassel-Marcus (RRKM) theory.[9] The calculated RRKM rate constants are consistent with the time scale of the prompt first bond breakage (< 200 fs).[24, 26] However, such a theoretical finding is only valid if a) the $S_1 \rightarrow T_1$ ISC process is much faster than the prompt bond dissociation and b) the

energy redistribution among all the vibrational modes is completed within 100 fs. Therefore, the fundamental problem for the photodissociation dynamics of acetone on the $S_1(n,\pi^*)$ surface still remains controversial.

The goal of the present study is to shed new light on the femtochemistry of Norrish type-I reaction of acetone using femtosecond pump–probe mass spectrometry in combination with high-level ab initio/density functional theory (DFT) calculations. The present study further clarifies the ambiguity of the "mixed $\{S_1,T_1\}$ surface" that was widely adopted as a theoretical foundation to describe the reaction mechanism and the related dynamics for acetone (see, for example, refs. [16, 20, 24c, 26a]). The paper is organized in two parts. First, we report real-time observation of the α-cleavage reaction dynamics of isolated acetone upon excitation to the $S_1(n,\pi^*)$ state. Second, we focus on the theoretical approach to further provide a clear mechanistic picture for the photochemistry of acetone taking place on the multidimensional S_1 PES. Moreover, the S_1 α-cleavage energy barrier of six other aliphatic ketones (Scheme 1 in Section 3.6) are also characterized and compared with that of acetone.

Experimental Section

The experimental apparatus for femtosecond pump and probe time-of-flight (TOF) mass spectrometry has been described in detail elsewhere.[68, 69] Briefly, the laser system contains a colliding-pulse mode-locked (CPM) laser pumped by an Ar^+ laser and then amplified by a four-stage, Nd:YAG-pumped amplifier operating at 20 Hz. The output of the fs laser source has a pulse width of $\sim$80 fs with pulse energy of $\sim$150 μJ at 615 nm. The pulse was split to provide the pump and probe beams. For the pump, the 615 nm output was frequency doubled. The probe beam was passed to a computer-controlled translation stage for the time delay. The instrumental response function was determined by in situ measurements.[68–70] The two beams were spatially combined and focussed onto the supersonic molecular beam inside the vacuum chamber containing the TOF mass spectrometer. By gating the signal due to a particular ion and varying the delay time between pump and probe beams, the transient of each species was measured.

Acetone (99%, Aldrich) was used without further purification but its mass spectrum was consistent with literature values. The molecular beams were formed by expanding gaseous acetone seeded in He to give a total stagnation pressure of $\sim$140 kPa. The pulse nozzle was heated to $\sim$130 $^\circ$C to prevent clustering of molecules during expansion.

2. Results and Analysis

Figure 2 shows the femtosecond mass spectra for A) [D_0]acetone and B) [D_6]acetone. Both mass spectra are similarly characterized by two peaks corresponding to the parent ion (58 and 64 amu for [D_0]- and [D_6]acetone, respectively) and the fragment ion (43 and 46 amu for [D_0]- and [D_6]acetone, respectively). Figure 3 A displays the time dependence (transient) of the parent ions (58 amu and 64 amu), whereas Figures 3 B and 3 C show the fragment transients at 43 and 46 amu for [D_0]- and [D_6]acetone, respectively. Only a spikelike signal is indicated in the transients of the parent ion (Figure 3 A), so the parent transients are fitted
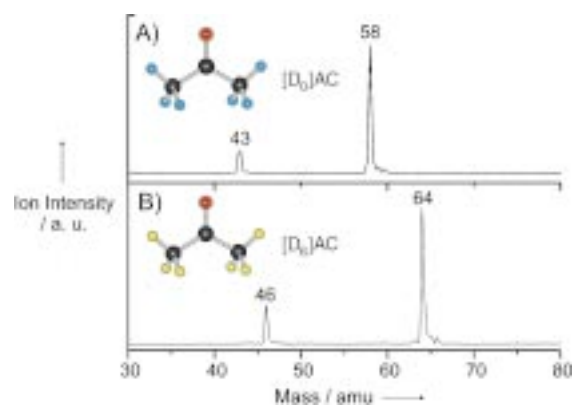

Figure 2. Femtosecond mass spectra of A) [D_0]acetone and B) [D_6]acetone. The spectra were obtained at a delay time of $\sim$50 fs between the pump and probe pulses. Note that the ion signal at the cluster masses (for example 116 amu for the [D_0]AC dimer, not shown) is negligible.
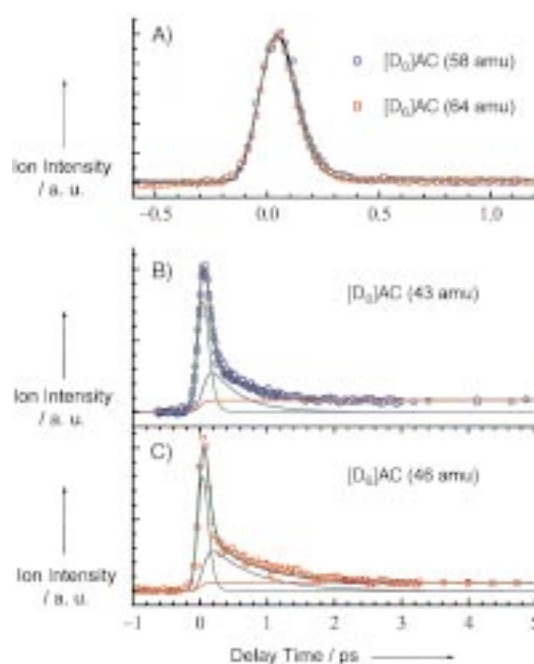

Figure 3. A) Transients of [D_0]acetone at 58 and [D_6]acetone at 64 amu. B) Fragment transient of [D_0]acetone at 43 amu. C) Fragment transient of [D_6]acetone at 46 amu. All transients were taken under the conditions of $\sim$0.5 μJ pump and $\sim$20 μJ probe pulse energies. The fragment transients (B and C) are fitted with three different components as indicated (see text).

to a single exponential decay function (time constant $\tau \sim 50$ fs) with convolution of the instrumental response function (Gaussian, FWHM $\sim$170 fs). The fragment transients, as shown in Figures 3 B and 3 C for [D_0]- and [D_6]acetone, respectively, feature three independent components. The first one is a fast-decay component with a pulse-limited decay time constant ($\sim$50 fs) similar to the spike shown in the parent transients. The second one is a rise and decay component that can be described by time constants on the sub-ps time scale ($\sim$50 fs and 500 fs), which describes the fragmentation of acetone to acetyl and methyl radicals.[21] The third one is characterized by a constant "offset" signal which is persistent on the ps and sub-ns time scale

(Figure 4). All transients were taken under the condition of medium pump intensity (pulse energy $\sim 0.5\,\mu J$) and relatively high probe intensity (pulse energy $\sim 20\,\mu J$).

Figure 4. A) Extended fragment transients for [D_0]acetone (lower trace) and [D_6]acetone (upper trace). The baseline of the [D_6]acetone transient has been vertically shifted for clarity. B) Pump-laser power dependence ($0.3\,\mu J <$ pump pulse energy $< 1.0\,\mu J$) of [D_0]acetone taken at 43 amu with two different delay times and the corresponding slopes as indicated (probe pulse energy $\sim 20\,\mu J$); see text for power dependencies.

Figure 5. Two pump – probe ionization schemes responsible for the observed transient signals of acetone. The absorption spectra shown on the left side are the experimental results adopted from refs. [29, 50]. The vertical transitions and the corresponding oscillator strengths (f) shown on the right side were calculated using the TDDFT method at the B3P86/6-311 $++G(d,p)$ level of theory.

Figure 5 shows two different pump – probe schemes that may contribute to the observed transient signals of acetone ($\lambda_{ex} =$ 307 and $\lambda_{probe} = 615$ nm). The solid arrows describe the one-pump-photon excitation followed by three-probe-photon ionization process, whereas the dashed arrows represent the two-pump-photon excitation plus one-probe-photon ionization process. It will be detailed in the subsequent paper[38] that the contribution of the transient signals from the one-photon excitation process (requiring two more probe photons than the two-photon excitation process) can be minimized under the condition of very low probe intensity (for example, pulse energy $\sim 2\,\mu J$) so that the dynamics resulting from the two-photon excitation process can be effectively isolated and studied.[21] On the other hand, the S_1 dynamics due to the one-photon excitation may be observed using high probe intensity (pulse energy $\sim 20\,\mu J$). Even though both one- and two-photon excitation processes are involved with high probe intensities, the dynamics of both processes may occur on different time scales so that they can be studied separately. Indeed this is the case for our experiments on acetone.

Figure 4 A shows the extended time dependence of the fragment ions under high probe intensity for [D_0]- and [D_6]acetone, respectively. Apparently, a component is still rising for pump – probe delay times up to 120 ps. Figure 4 B demonstrates the pump-laser power dependence at constant probe

intensity (pulse energy $\sim 20\,\mu J$) for [D_0]acetone (43 amu) at $t =$ 50 fs and 50 ps shown as upper and lower traces, respectively. At $t = 50$ fs, the observed slope is 1.07 ± 0.02. At $t = 50$ ps, however, the observed slope is only 0.73 ± 0.04. Therefore, the source of the slow-rising component is clearly different from that of the fast-decay spike in the fragment transients. Under the condition of low probe intensity (pulse energy $\sim 3\,\mu J$), the pump-laser power dependence of the parent transient (58 amu) was measured to be 1.30 ± 0.02 at $t = 50$ fs, to indicate the major contribution to the signal from a two-photon excitation process through an intermediate state (Figure 5). The power-dependence measurements have demonstrated that the spike signal shown in the fragment transients must be due to both one- and two-photon excitation processes *but the slow-rising signal can only result from the one-photon process.*

The slow-rising signal shown in the fragment transients (Figure 4 A) can be simulated by a simple kinetic model with two contributions: one decays while the other increases. The fact that the observed signal is rising rather than decaying indicates that the effective ionization cross-section (ionization probability) of the increasing component is larger than that of the decay component. Since our excitation energy (93 kcal mol^{-1}) is above or very close to the reported dissociation threshold (91.5 or 93.5 kcal mol^{-1}),[13, 34] the observed increasing signal should be due to the generation of the acetyl radical after the α-cleavage

on the T_1 surface [Eq. (1)]. To fit the fragment transient data shown in Figure 4A, we assume the rate-limiting step to be the $S_1 \rightarrow T_1$ ISC process and use the same time constant for the decaying and the increasing components according to the reported S_1 lifetime.[39] As a result, the amplitude of the increasing component (corresponding to the acetyl radical) was determined to be larger than that of the decay component (corresponding to the S_1 species) by a factor of ~ 15. Note that this amplitude ratio was fitted to give the same result for both [D_0]- and [D_6]acetone.[40] The high amplitude ratio between the increasing and the decaying components is mainly due to the resonant-enhanced property of the multiphoton ionization for the acetyl radical but not for the S_1 species.[41] Moreover, the fragmentation in the ionic channel through the intense probe pulse for the S_1 species should also be considered. Since the parent transients (Figure 3A) do not indicate any significant offset or long-decay component, ionization of the S_1 species under our experimental conditions should efficiently lead to fragmentation in the ionic channel and give the corresponding ion signal in the fragment mass. Thus, the ionization probability of the acetyl radical is expected to be larger than that of the S_1 species by one order of magnitude according to our observation and analyses.

The above experimental findings imply two important points regarding the dynamic behavior of acetone upon one-photon excitation to the S_1 state. First, the fast-decay component due to one-photon excitation has a pulse-limited time constant (< 50 fs), which indicates a very rapid initial motion for the molecule to depart from the Franck–Condon (FC) region and head downhill on the S_1 surface (see below). Second, the slow-rising component shown in the fragment transients manifests the birth of the acetyl radical resulting from the one-photon excitation. This direct evidence strongly supports the early fluorescence results[29, 33] that *the lifetime of S_1 acetone is on the nanosecond time scale*. In other words, the first α-CC bond dissociation of acetone upon excitation to the S_1 state *cannot* be prompt. It is very important to note that all the relevant fs-resolved mass spectroscopic studies, including this and many other recent investigations,[22, 24, 26] give essentially *the same* experimental results (see, for example, Figure 3). However, our extended time-dependence (Figure 4A) and power-dependence (Figure 4B) measurements are the key pieces of evidence to unravel the controversy for the reported S_1 dynamics of acetone. In the following, we will provide more theoretical results to further support our experimental findings.

3. Theoretical Calculations

3.1. Methods

Two theoretical approaches, the spin-unrestricted (U) DFT[42] and the CASSCF[43] methods, were employed in order to appropriately describe the ground-state bond-dissociation minimum-energy pathway (MEP) of acetone. For the UDFT method, the geometry of each species along the bond-breaking RC was optimized using the UB3LYP hybrid functional[44, 45] with the

6-31G(d) basis set.[46] Since the S_0 acetone is a closed-shell species, the spin-restricted (R) Kohn–Sham (KS) orbitals were implemented to describe the PES around the S_0 equilibrium region. As the CC bond stretches to an extent where the RKS and UKS descriptions start to differ (the RKS/UKS instability or symmetry breaking point),[47] the UKS orbitals were used to better describe the bond dissociation process. This spin-unrestricted DFT approach, although in principle suffers spin contamination from higher-multiplicity excited states, may well characterize the bond-dissociation PES for acetone and offer an economical alternative to other, more elaborate multiconfiguration (MC) SCF and higher-order correlation methods.[47]

To correctly describe the bond-dissociation as well as the excited-state PESs of acetone, a MCSCF scheme was implemented using the CASSCF approach. The idea of CASSCF is to have an active space well chosen and then perform full configuration interaction calculations inside the active space. Our strategy is to define a proper active space which is capable of describing the bond-dissociation processes and the n,π^* excited states of acetone. An active space with ten electrons distributed among eight orbitals was chosen throughout the CASSCF calculations. The total numbers of configurations generated in the adopted CAS(10,8) wavefunction are 1176 and 1512 for the S_1 (or S_0) and the T_1 states, respectively. The orbitals were first optimized at the Hartree–Fock (HF) level and then properly selected into the active space for the following CASSCF calculations. For example, two sets of C–C σ and σ^* orbitals, one set of C–O π and π^* orbitals, and two nonbonding orbitals of the oxygen atom were chosen in the active space for characterizing the PES near the S_0 minimum of acetone ($3a_1 + 2b_1 + 3b_2$ in C_{2v} symmetry or $6a' + 2a''$ in C_s symmetry; Figure 6). For most of the MEP curves reported, a relaxed-surface scan was performed. The geometry of each species was optimized at the CAS(10,8)/6-31G(d) level along a certain coordinate (for example, single α-CC bond-breaking RC, synchronous α-CC two-bond-breaking RC, CO out-of-plane bending coordinate, CCO bending coordinate, and so forth) with a small step size (bond lengths in 0.05 Å, and bond or dihedral angles in $5°$). Finally, a two-dimensional PES was constructed using the time-dependent (TD) DFT method[48, 49] with the single-point energy calculated at the TD-B3LYP/6-31G(d) level using the interpolated geometry originally optimized at the CAS(10,8)/6-31G(d) level.

For all stationary points, vibrational frequencies were calculated at the same level of theory as the geometry optimization in order to determine the nature of the stationary points and to provide zero-point energy (ZPE) corrections for the PES. To confirm that the TS is the correct saddle point connecting two local minima, intrinsic reaction coordinate (IRC) calculations were performed. Furthermore, single-point energy calculations were carried out for each stationary point at the (TD or U) B3P86/6-311 $++$ G(d,p)//CAS(10,8)/6-31G(d) level of theory (TDDFT for the S_1 PES, and UDFT for both S_0 and T_1 PESs). The vertical excitation energies and the oscillator strengths of acetone calculated at the TD-B3P86/6-311 $++$ G(d,p) level are represented in Figure 5 together with the experimental absorption spectra of the n $\rightarrow \pi^*$ transition[29] and the higher electronic
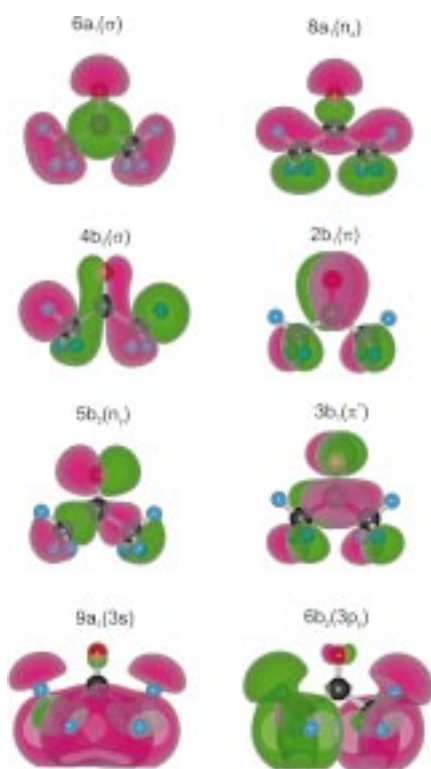
Figure 6. *The optimized HF/6-31G(d) orbitals in C_{2v} symmetry used as the starting active space in the CASSCF(10,8)/6-31G(d) calculations for acetone near its S_0 minimum.*

transitions involving Rydberg states[50] for comparison. The CASSCF optimized structures of acetone on the S_0, S_1, and T_1 surfaces are shown in Figures 7 and 8; the results for the energetics of each species are summarized in Table 1. All of the electronic structure calculations reported were performed using the Gaussian software package.[51]

3.2. The Ground-State Potential Energy Surface

The simple homolytic bond-breaking process without involving a reverse energy barrier has been a subject in many important

radical – radical association reactions.[52] A good description of such a bond-dissociation curve is crucial to accurately determine the reaction rates using variational RRKM theory.[52, 53] In a simple example, the O–H bond dissociation of water illustrates how the shape of a PES varies with different theoretical levels applied.[47] For acetone, the ground-state single α-CC bond-rupture reaction produces acetyl and methyl radicals. The description of the bond-dissociation curve of acetone is far more complicated than that of water because many other internal degrees of freedom need to be considered. Therefore, a relaxed-surface scan is necessary to describe the MEP of acetone along the single α-CC bond-dissociation RC.

3.2.1. The Single α-CC Bond-Breaking MEP (C_s)

The equilibrium geometry of S_0 acetone has C_{2v} symmetry with the z-axis along the CO double bond and the skeleton of the molecule lying in the (y, z) symmetry plane. Starting from the S_0 C_{2v} minimum along the single α-CC bond-breaking RC, the MEP of acetone was successfully characterized at the UB3LYP/6-31G(d) and the CAS(10,8)/6-31G(d) levels of theory and the relevant internal coordinates and the relative classical energies (i.e., without ZPE corrections) are shown in Figures 9 A and 9 B, respectively. Several important features of the calculated MEP curves are noteworthy. First, the RB3LYP energy (shown as a dashed line in Figure 9 B) continues to increase as the α-CC bond stretches since it gives the wrong dissociation limit, while the UB3LYP energy converges to a value ~ 86.3 kcal mol^{-1}. The symmetry breaking point occurs at RC ~ 2.6 Å, where the energy calculated at the RB3LYP level starts to be higher than that calculated at the UB3LYP level. Second, the MEP characterized using the UDFT method is similar to that using the CASSCF method. As shown in Figure 9 B, the DFT curve (open circles) is slightly lower in energy than the CASSCF curve (filled circles) for 1.5 Å $<$ RC < 2.5 Å, but the former becomes slightly higher in energy than the latter at RC > 2.5 Å. In particular, while approaching the asymptotic bond-dissociation limit (RC > 5 Å), the relative energy calculated through UDFT is higher by only 2 kcal mol^{-1} than that predicted by CASSCF. Third, there is a very
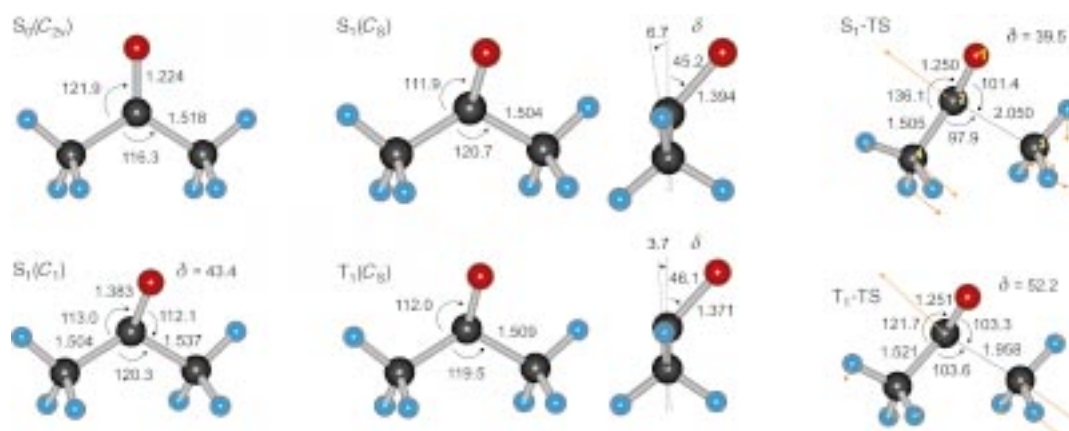

Figure 7. *The structures of the $S_0(C_{2v})$, $S_1(C_1)$, $S_1(C_s)$, $T_1(C_s)$, S_1-TS, and T_1-TS species optimized at the CASSCF(10,8)/6-31G(d) level of theory with corresponding bond lengths [Å] and bond angles [°] as indicated. The CO out-of-plane bending angle is defined as $\delta = 180° -$ D, where D is the dihedral angle of $O_1C_2C_3C_4$.*
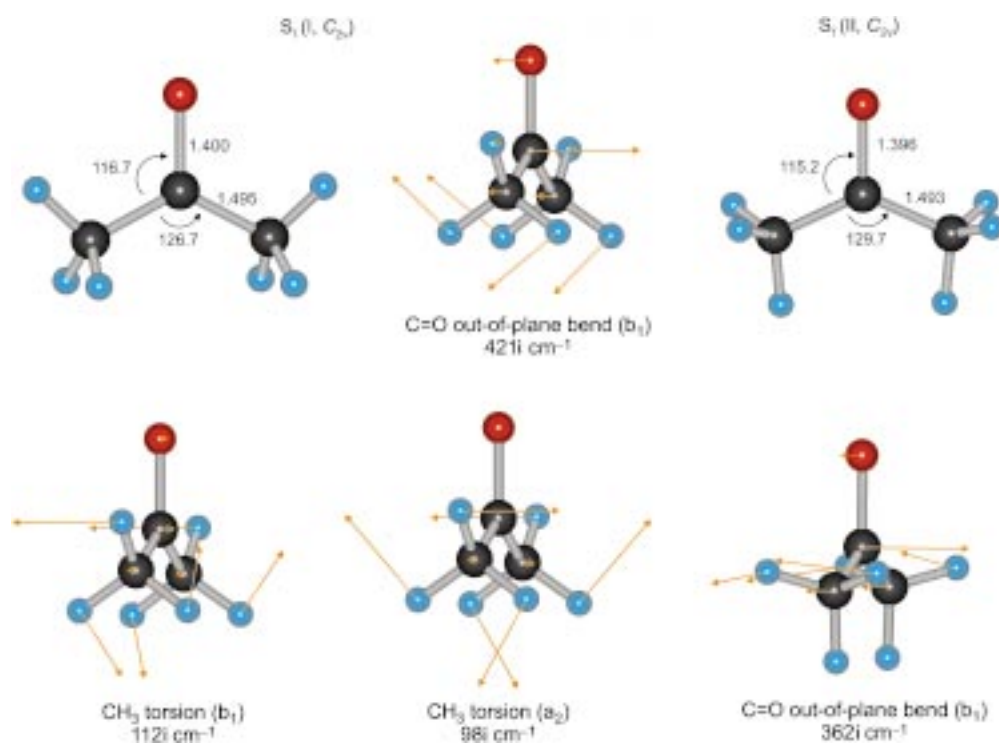
Figure 8. *The optimized structures of the $S_1(I, C_{2v})$ and the $S_1(II, C_{2v})$ species. The vectors represent the normal-coordinate motions corresponding to the imaginary frequencies of each species.*

Furthermore, the RB3LYP energy (shown as a dashed line in Figure 10 B) continues to increase as the two CC bonds stretch whereas the UB3LYP energy converges to a value of 106.5 kcal mol^{-1}. The RKS/UKS symmetry breaking point occurs at RC ∼ 2.3 Å, which is slightly shorter than the single bond-dissociation MEP. Furthermore, a shallow local minimum (van der Waals complex) was found at RC = 3.258 Å with a corresponding TS at RC = 2.725 Å, as clearly seen in the inset of Figure 10 B.

3.3. The Excited-State Potential Energy Surfaces

3.3.1. The C_{2v} S_1 Structures

By constraining the C_{2v} symmetry as for the S_0 minimum species and optimizing its geometry in the S_1 state, a structure with the C=O bond length increasing from 1.224 [$S_0(C_{2v})$] to 1.400 Å

shallow minimum located in the long range of the simple α-CC bond-breaking MEP of acetone. This feature can be clearly seen in the extended window inside Figure 9 B.[54]

3.2.2. The Concerted α-CC Two-Bond-Breaking MEP (C_{2v})

The ground-state concerted bond-dissociation MEP of acetone was constructed by synchronously stretching both α-CC bonds from the S_0 minimum along the two-bond-breaking RC while maintaining the C_{2v} symmetry throughout the whole dissociation curve. The results calculated at the B3LYP/6-31G(d) level are shown in Figure 10. Similar to the single α-CC bond-breaking MEP, the predicted concerted bond-dissociation MEP involves no intrinsic reverse energy barrier with respect to dissociation.

[S_1, C_{2v})] was obtained (Figure 8 left). The lengthening of the CO bond exhibits the nature of the n → π* transition, where the carbonyl moiety attempts to reduce its π-bonding character upon excitation to the S_1 state. Furthermore, normal-mode analysis of the $S_1(I, C_{2v})$ species indicates the existence of three imaginary frequencies, one corresponds to the CO out-of-plane wagging motion (b_1), while the other two correspond to synchronous and asynchronous CH$_3$ torsional motions (b_1 and a_2). As shown in the left panel of Figure 8, all three vibrational motions intend to break the symmetry out of the (y, z) plane, suggesting the existence of other stationary points with energies lower than $S_1(I, C_{2v})$ on the S_1 surface if one follows the directions of the vibrational motions corresponding to those imaginary frequencies.

Table 1. *Total energy E [hartree] and relative energy ΔE [kcal mol^{-1}] for the minima, transition states, and conical intersection of acetone on the S_0, S_1, and T_1 surfaces.*

species	E CASSCF[a]	ZPE[a,b]	ΔE CASSCF[a,c]	E DFT[d]	ΔE DFT[c,d]	ΔE Exp.
S_0 (C_{2v})	− 192.07105	55.9	0.0	− 193.78815	0.0	
S_1 (I, C_{2v})	− 191.90931	53.7	99.2	− 193.63267	95.3	
S_1 (II, C_{2v})	− 191.91180	54.2	98.1	− 193.63587	93.8	
S_1 (C_s)	− 191.91855	55.0	94.7	− 193.63722	93.7	87.0[55]
S_1 (C_1)	− 191.91458	54.7	96.9	− 193.63781	93.0	
S_1-TS	− 191.87703	52.4	118.2	− 193.60377	112.1	
S_0/S_1 CI	− 191.87821		117.5[e]			
T_1 (C_s)	− 191.92673	55.0	89.6	− 193.65263	84.1	
T_1-TS	− 191.89875	52.5	104.7	− 193.64011	89.5	93.5[34d]/91.5[13]

[a] CASSCF(10,8)/6-31G(d). [b] Zero-point energy [kcal mol^{-1}]. [c] With ZPE corrections. [d] (TD) B3P86/6-311 + + G(d,p)//CASSCF(10,8)/6-31G(d). [e] ZPE adopted from S_1-TS.
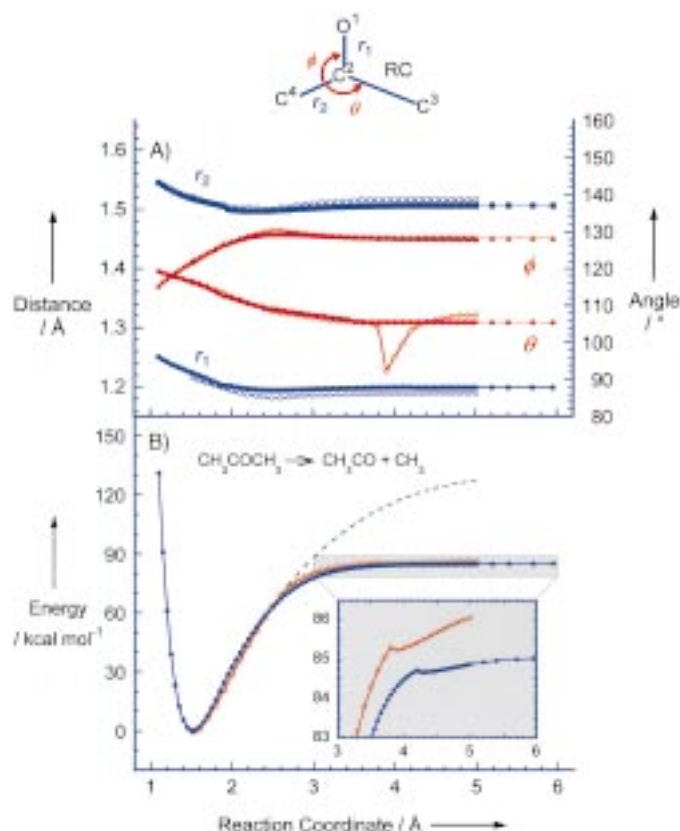
Figure 9. A) The geometry parameters of acetone optimized at the CASSCF(10,8)/6-31G(d) level (filled symbols) and the UB3LYP/6-31G(d) level (open symbols) along the single α-CC bond-breaking RC on the ground-state surface with constraint of the (y, z) symmetry plane (the OCCC molecular symmetry plane) throughout the MEP (C_s). B) The corresponding S_0 α-CC bond-dissociation MEP of acetone with the shallow minimum feature enlarged in the inset. The energies are related to the S_0 minimum.

Figure 10. A) The geometry parameters of acetone optimized at the UB3LYP/6-31G(d) level along the synchronous α-CC two-bond-breaking RC on the ground-state surface. B) The corresponding MEP with the shallow minimum feature shown in the inset. The energies are related to the S_0 minimum.

Further release of the constraint of the torsional degrees of freedom for the methyl groups and optimizing the geometry from the S_1(I, C_{2v}) species, another stationary point [S_1(II, C_{2v})] on the S_1 surface was obtained (Figure 8, right). The S_1(II, C_{2v}) species also has C_{2v} symmetry but differs from the S_1(I, C_{2v}) species in three major aspects. First, both structures are different in the torsional angles of the methyl groups, namely the methyl groups with respect to the carbonyl group are in an "eclipsed" configuration for S_1(I, C_{2v}) but are "staggered" for S_1(II, C_{2v}). Second, the classical energy of S_1(II, C_{2v}) is lower by 1.6 kcal mol^{-1} compared to that of S_1(I, C_{2v}). Third, the vibrational frequencies of the S_1(II, C_{2v}) species only involve one imaginary value, which corresponds to the CO out-of-plane wagging motion (b$_1$). Therefore, the internal rotations of the methyl groups in acetone must be one of the driving forces to be considered upon excitation to the S_1(n,π^*) state. The most favorable C_{2v} structure of the S_1 acetone has been calculated to be the S_1(II, C_{2v}) species because of the hyperconjugative interactions between the hydrogen atoms of the methyl groups and the unpaired p orbitals of the excited carbonyl functional group in the S_1 state of acetone. However, this planar S_1(II, C_{2v}) species still involves one imaginary frequency, to indicate that S_1(II, C_{2v}) is in nature a transition state (first-order saddle point) on the S_1 PES. The

nature of a b$_1$ imaginary frequency of the S_1(II, C_{2v}) species suggests that the true minimum on the S_1 surface may be located by relaxing the original C_{2v} geometry out of the (y, z) plane but still preserving the (x, z) symmetry plane.

3.3.2. The Pyramidal MEP and the S_1 Minimum (C_s)

The pyramidal MEP of acetone on the S_1 surface was constructed through a relaxed-surface scan along the eigenvector direction corresponding to the CO out-of-plane wagging motion of the S_1(II, C_{2v}) TS. Figure 11 shows the S_1 MEP together with the S_0 energy curve along the CO out-of-plane bending (or pyramidal) coordinate (δ, as defined in Figure 7). The S_1 pyramidal MEP is characterized by a symmetrical double-well potential with two minima [S_1(C_s)] located around $\delta = \pm 45°$. The inversion energy barrier at $\delta = 0°$ is determined to be the energy difference between S_1(II, C_{2v}) and S_1(C_s) on the MEP, which was calculated to be 4.2 kcal mol^{-1} at the CAS(10,8)/6-31G(d) level of theory (without ZPE corrections). Further single-point energy calculation at the TD-B3P86/6-311 ++ G(d,p) level substantially reduced the value down to 0.85 kcal mol^{-1} (Table 1), which is comparable to the experimental inversion barrier height (1.4 kcal mol^{-1}).[32] At large pyramidal angles, the S_0 and S_1 curves rapidly approach each other along the δ coordinate, which indicates the existence of an S_0/S_1 surface-crossing point around that pyramidal angle
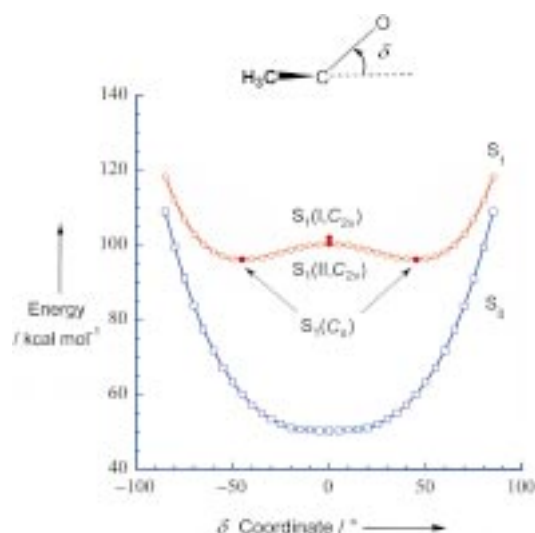
Figure 11. *The S_1 CO out-of-plane bending (δ) MEP of acetone optimized at the CASSCF(10,8)/6-31G(d) level with constraint of the (x, z) symmetry plane throughout the MEP (C_s). The energies are related to the S_0 minimum.*
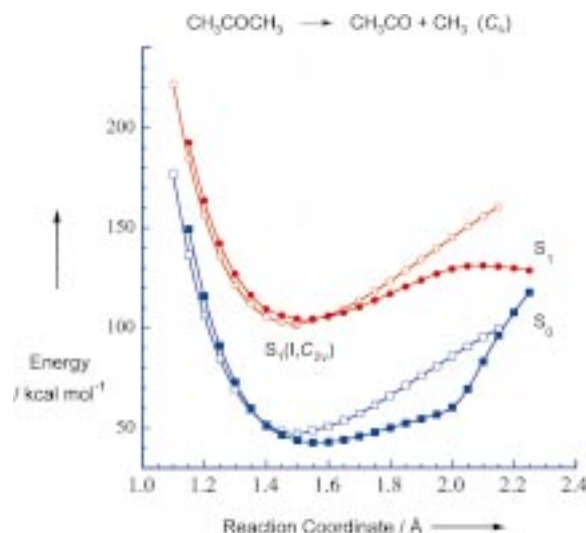

Figure 12. *The S_1 single α-CC bond-dissociation MEP of acetone optimized at the CASSCF(10,8)/6-31G(d) level with constraint of the (y, z) symmetry plane throughout the MEP (C_s). Note that the MEP is described by two different curves; the open circles at RC < 1.6 Å and the filled circles at RC $\geq$ 1.6 Å (see text). The energies are related to the S_0 minimum.*

region. In fact, such a surface intersection point has been reported to have a highly bent structure with a CO bond length of 1.77 Å and a pyramidal angle δ of $\sim 77°$ optimized at the CAS(8,7)/6-31G(d) level of theory.[11]

The geometry of the $S_1(C_s)$ minimum was fully optimized at the same CASSCF level, and its structure is shown in Figure 7. The frequency calculation indicates that the $S_1(C_s)$ species is a true minimum on the S_1 surface because all the vibrational frequencies are real numbers. The most relevant features of the $S_1(C_s)$ structure are the CO bond length and the CO out-of-plane bending angle δ, which were determined to be 1.394 Å and 45.2°, respectively. Using a large active space with a triple-zeta basis set, the optimized $S_1(C_s)$ geometry was reported to have a CO bond length of 1.355 Å and a CO out-of-plane bending angle of 47.6°.[31] On the other hand, the equilibrium CO out-of-plane bending angle of the $S_1(C_s)$ species was fitted to a value of only 25° according to the jet-cooled fluorescence spectrum data.[32, 55]

3.3.3. The S_1 Single α-CC Bond-Dissociation MEPs (C_s and C_1)

The minimum-energy reaction pathway for α-cleavage of acetone on the S_1 surface has been studied via the relaxed-surface scan for the S_1 species along the single α-CC bond-breaking RC. Two approaches were implemented. The first one starts from the S_1(I, C_{2v}) species while retaining the C_s symmetry with respect to the (y, z) plane throughout the bond-dissociation MEP (Figure 12). The second one starts from the $S_1(C_s)$ minimum species so that the symmetry of the molecular geometry is reduced to C_1 along the bond-breaking RC. The results of the second approach for the optimized geometry parameters and the energy curves are shown in Figures 13 A and 13 B, respectively. Even though the first (C_s) and the second (C_1) bond-dissociation MEP curves are very similar in shape, the relative energy for the S_1 state of the former is in general higher than that of the latter by 5 – 10 kcal mol^{-1} due to the extra symmetry
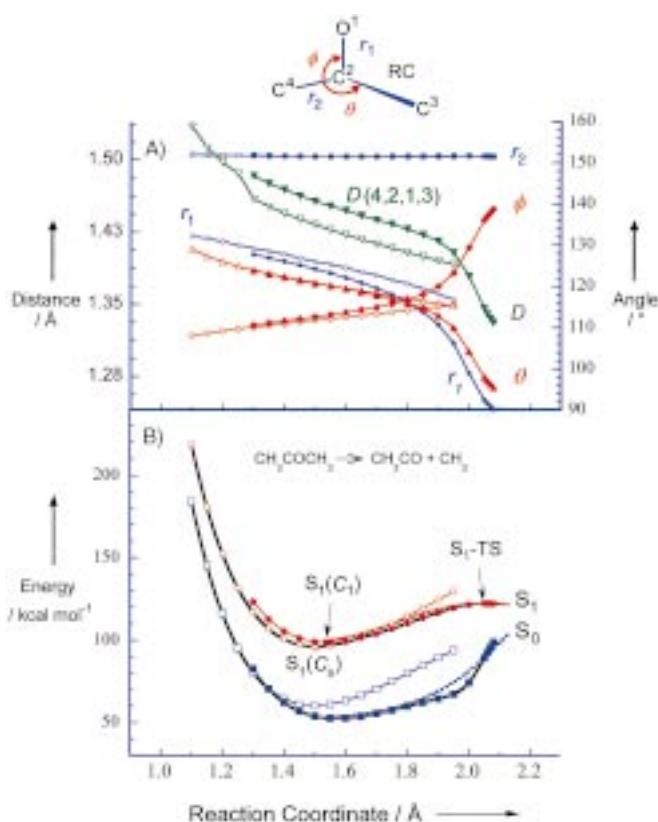
Figure 13. *A) The geometry parameters of acetone optimized at the CASSCF(10,8)/6-31G(d) level along the S_1 single α-CC bond-breaking RC without symmetry constraint (C_1). The open and filled symbols respectively represent the corresponding geometry parameters for the two different curves described below. B) The corresponding S_1 α-CC bond-dissociation MEP of acetone. Note that the MEP is described by two different curves; the open circles at RC < 1.65 Å and the filled circles at RC $\geq$ 1.65 Å. The dotted curves are those obtained from the mass-weighted IRC calculations. The energies are related to the S_0 minimum.*

constraint of the former. As a result, the following discussion will only focus on the second (C_1) MEP.

The whole S_1 single α-CC bond-dissociation MEP is comprised of two different curves. The first curve of the MEP was calculated starting from the $S_1(C_s)$ geometry and the corresponding active space with C_1 symmetry along the RC in the range of 1.1 – 1.95 Å (shown as open circles in Figure 13 B). For the second curve of the MEP, the active space was prepared at a longer CC bond separation (for instance, RC = 1.8 Å) based on a prior HF calculation and the minimum energy curve was further calculated along the RC in the range of 1.3 – 2.08 Å (shown as filled circles in Figure 13 B). Note that the α-CC bond-dissociation MEP (C_1) can be best represented by the first curve for the RC less than 1.65 Å and by the second curve for the RC greater than 1.65 Å.

Along the second curve on the S_1 surface (Figure 13 B), the bond-dissociation MEP is characterized by a minimum point [$S_1(C_1)$] and a saddle point (S_1-TS) at RC = 1.54 and 2.05 Å, respectively. Differing from $S_1(C_s)$, the $S_1(C_1)$ species has an asymmetrical structure with two different CC bond lengths (1.504 and 1.537 Å) and a CO out-of-plane bending angle δ of 43.4° (Figure 7). On the other hand, the geometry of the S_1-TS species is characterized by a substantially lengthened CC bond length (2.050 Å) and a widely bent CCO angle (136.1°). Note that the current result for the structure of the S_1-TS is similar to that calculated at the lower CAS(8,7)/6-31G(d) level.[11] Normal coordinate force-constant calculations indicate that all the vibrational frequencies are real numbers for the $S_1(C_1)$ species but there is one (and only one) imaginary frequency (657i cm^{-1}) corresponding to the asymmetric CC stretching motion (the α-CC bond-breaking RC) of the S_1-TS species. Therefore, it is confirmed that the $S_1(C_1)$ species is another local minimum on the S_1 surface, and the S_1-TS species corresponds to a transition state leading to the α-CC bond cleavage process responsible for the Norrish type-I reaction of acetone on the S_1 PES.

The energetics (with ZPE corrections) for both $S_1(C_s)$ and $S_1(C_1)$ species are similar; the former is lower in energy than the latter by 2.2 kcal mol^{-1} at the CASSCF level but the latter is slightly more stable at the TDDFT level (Table 1). On the singlet surface, the relative CASSCF energies of $S_1(C_s)$ and S_1-TS are 94.7 and 118.2 kcal mol^{-1}, respectively, with regard to the $S_0(C_{2v})$ species. On the triplet surface, the relative CASSCF energies of $T_1(C_s)$ and T_1-TS are 89.6 and 104.7 kcal mol^{-1}, respectively. At the CASSCF(10,8)/6-31G(d) level of theory, the energy barriers corresponding to the α-cleavage process on the S_1 and the T_1 surfaces are 23.5 and 15.1 kcal mol^{-1}, respectively. The energy barrier of the S_1-TS is reduced to 18.4 kcal mol^{-1} and that of T_1-TS is drastically reduced to 5.4 kcal mol^{-1} based on a TD-UB3P86/6-311++G(d,p) or UB3P86/6-311++G(d,p) single-point calculation at the CASSCF optimized geometry. It is worth noting that the dissociation threshold on the T_1 surface (determined by the T_1-TS species) predicted by the UDFT approach (89.5 kcal mol^{-1} above S_0) is in better agreement with the experimental result (91.5 kcal mol^{-1}, or 93.5 kcal mol^{-1} above S_0)[13, 34] than that obtained using the MRMP2 method (87.8 kcal mol^{-1} above S_0).[9] On the other hand, the theoretical predictions of the $S_0 \rightarrow S_1$ 0-0 transition were overestimated by 7.7 and

6.0 kcal mol^{-1} at the CASSCF and the TDDFT levels, respectively, in comparison with the jet-cooled fluorescence results (87 kcal mol^{-1} above S_0).[32, 55]

In addition to the relaxed-surface scan for the MEP shown in Figure 13, we have also performed mass-weighted IRC calculations starting from the S_1-TS species so that the reaction path on the S_1 surface can be followed according to the direction of the normal-coordinate vector shown in Figure 7. The energy curves for the calculated S_1 IRC reaction path and the corresponding S_0 path are shown in Figure 13 B as dotted traces. On one side, the $S_1(C_1)$ minimum is approached by following the "forward" direction of the IRC path corresponding to the shortening of the α-CC bond distance. On the other side, the difficulties of optimizing the CASSCF orbitals were encountered when following the IRC path in the "reverse" direction at IRC < − 0.04 bohr amu$^{1/2}$. While following the reverse IRC path from the S_1-TS to the last point where the CASSCF optimization is successful, the total energy was lowered by only 0.7 kcal mol^{-1} but the S_0/S_1 energy gap shrunk substantially from 32.9 to 15.9 kcal mol^{-1} (Figure 13 B). The failure of the S_1 state-specific CASSCF optimization after IRC < − 0.04 bohr amu$^{1/2}$ is the result of the breakdown of the Born – Oppenheimer approximation in describing the adiabatic S_1 PES when the S_0 surface rapidly approaches the S_1 surface along the bond-breaking RC. This feature will be discussed in greater detail in the next Section.

3.3.4. The S_1 Concerted Bond-Dissociation MEP (C_s)

Similar to the S_0 concerted MEP, the S_1 concerted CC bond-breaking MEP of acetone was constructed by synchronously stretching both α-CC bonds from the $S_1(C_s)$ minimum along the bond-breaking RC with C_s symmetry throughout the whole dissociation curve. As shown in Figure 14, two different curves are responsible for describing the MEP in the RC range of 1.1 – 3.0 Å based on our CASSCF approach. The key feature of the S_1 concerted MEP is that the energy on the S_1 surface continues to increase along the RC. This feature thus supports the non-concerted nature of the Norrish type-I reaction of ketones, namely, the bond dissociation of a ketone on the S_1 PES is not likely to occur in a concerted manner.

3.3.5. The S_1 CCO Bending MEP (C_1)

As illustrated in Figure 13 A, the geometry of the S_1 species along the single α-CC bond-dissociation MEP undergoes dramatic changes in the region of RC > 1.9 Å. The geometry parameters that change most prominently in that RC range are the CO bond length r_1, the CCO bending angle ϕ, the CCC bending angle θ, and the $C_4C_2O_1C_3$ dihedral angle D. The sharp decrease of the r_1 distance is due to the formation of the CO π-bond along the CC bond-breaking RC. On the other hand, the drastic increase of the ϕ angle causes the acetyl moiety to approach a linear CCO configuration in the longer RC region, further resulting in drastic variations for both θ and D angles. This approach towards a linear CCO configuration along the bond-breaking RC strongly suggests that the Norrish type-I reaction proceeds via the linear acetyl configuration. The corresponding state-correlation dia-
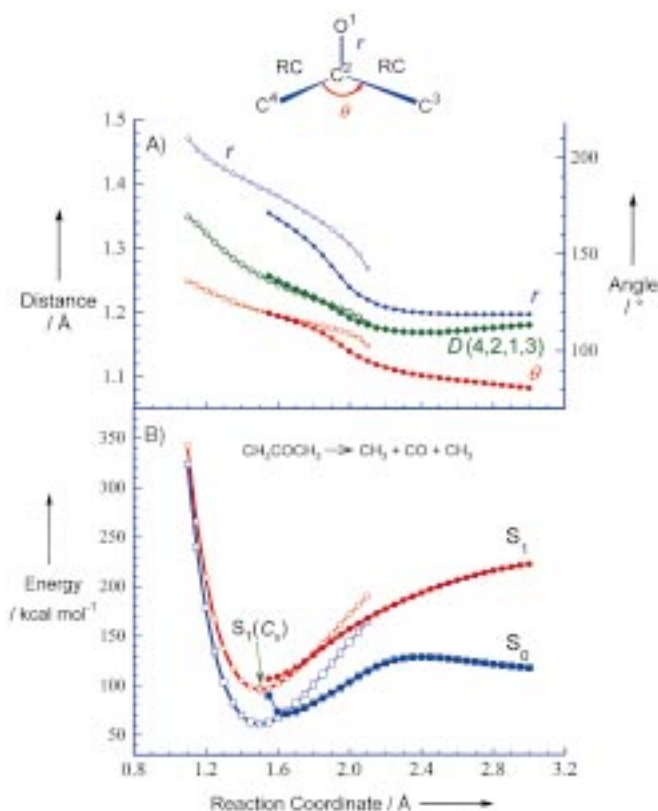
Figure 14. A) The geometry parameters of acetone optimized at the CASSCF(10,8)/6-31G(d) level along the S_1 synchronous α-CC two-bond-breaking RC with constraint of the (x, z) symmetry plane throughout the MEP (C_s). B) The corresponding S_1 synchronous bond-dissociation MEP of acetone. Note that the MEP is described by the open circles at RC $\leq$ 1.75 Å and the filled circles at RC > 1.75 Å. The energies are related to the S_0 minimum.
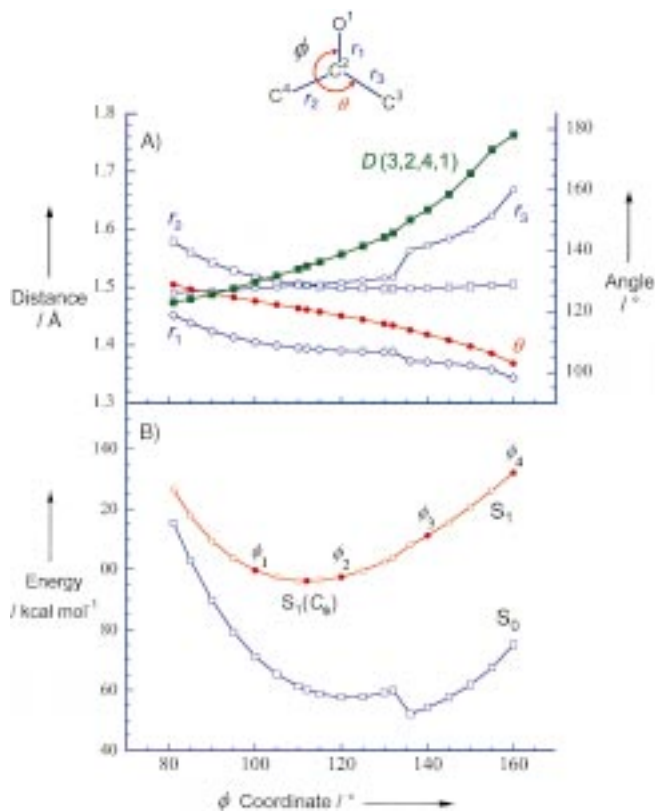

Figure 15. A) The geometry parameters of acetone optimized at the CASSCF(10,8)/6-31G(d) level along the CCO bending angle coordinate ϕ without symmetry constraint (C_1). B) The corresponding CCO bending MEP of acetone with ϕ_1, ϕ_2, ϕ_3, and ϕ_4 representing the species optimized at $\phi = 100°$, $120°$, $140°$, and $160°$, respectively. The energies are related to the S_0 minimum.

gram is shown in Figure 1. To further illustrate this key feature, we have performed a relaxed-surface scan to characterize the MEP along the CCO bending angle on the S_1 surface. The results for the optimized geometry parameters and the energy curves are shown in Figures 15 A and 15 B, respectively.

There are three important features in the CCO bending MEP. First, the MEP shows a bound-state feature on the S_1 surface with a minimum located at the $S_1(C_s)$ point. Second, the sudden geometrical change at $\phi \sim 135°$ along the S_1 MEP causes the corresponding S_0 energy to drop abnormally. Third, the S_1 bending MEP cannot be well characterized at larger bending angles because the α-CC bond dissociation was calculated to occur at $\phi > 160°$. The third feature readily manifests itself through the sharp increase in r_3 at $\phi > 150°$ as shown in Figure 15 A. Further relaxed-surface scans have also been carried out along the bond-dissociation RC on the S_1 surface at several different fixed bending angles ($\phi_1 - \phi_4$).

Five sets of different MEPs along the S_1 single α-CC bond-breaking RC with the fixed CCO bending angles of 100°, 120°, 140°, 160°, and 180° are shown in Figures 16 A – E, respectively. Note that the dotted traces shown in Figures 16 A and 16 B represent the different curves that are lower in energy at longer α-CC bond distances for the corresponding bending angles. Furthermore, the minima of Figures 16 A – 16 D, correspondingly

labeled $\phi_1 - \phi_4$, are the same points on the CCO bending MEP shown in Figure 15 B. The positions of those S_1 minima are shifted to longer distances along the bond-breaking RC as the CCO angle is increased from ϕ_1 (100°) to ϕ_4 (160°), whereas the corresponding saddle points on the S_1 surface move inward along the RC. At the bending angles larger than 160°, both the minimum and the saddle point approach each other along the bond-breaking RC and the S_1 MEP becomes repulsive in nature, as in the case of the linear CCO configuration demonstrated in Figure 16 E. This feature also explains why the relaxed-surface scan was not successful along the CCO bending MEP for ϕ values larger than 160° (Figure 15 B).

Now we return to the problem we encountered earlier during the IRC and the relaxed-surface scans along the S_1 single α-CC bond-dissociation MEP. That is, all the bond-breaking MEPs characterized at longer separations encountered the problem of convergence during the optimization of the state-specific CASSCF orbitals, because the S_0 surface rapidly approaches the S_1 surface along the bond-breaking RC and thus results in the breakdown of the Born–Oppenheimer approximation for describing the adiabatic S_1 PES. This result implies that we have to consider the sharply increased interaction between the S_1 and the S_0 surfaces while further following the RC and thus the state-average
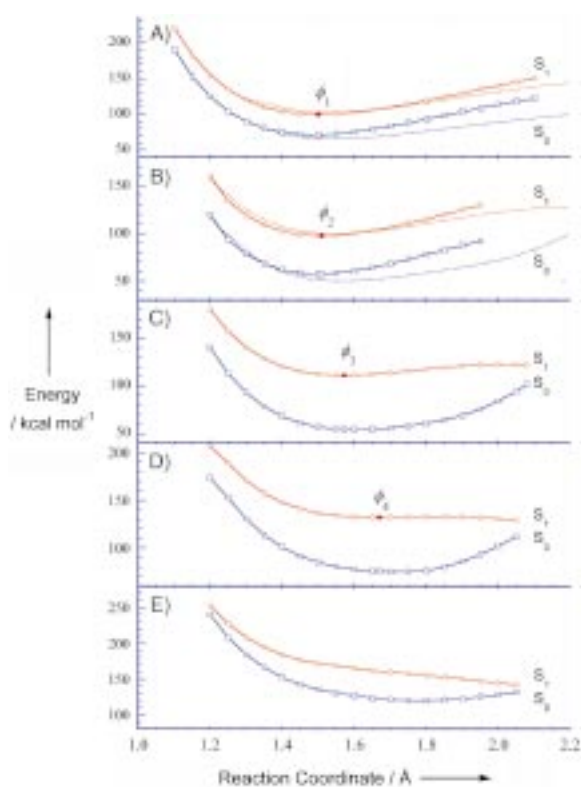
Figure 16. *The S_1 single α-CC bond-dissociation MEPs of acetone optimized at the CASSCF(10,8)/6-31G(d) level at the fixed CCO bending angles φ of A) 100°, B) 120°, C) 140°, D) 160°, and E) 180°. Note that the MEPs of (A) and (B) are described by two different curves. The energies are related to the S_0 minimum.*

CASSCF method should be implemented to search for the expected S_0/S_1 conical intersection (CI) at the lowermost surface crossing point.[56] The details for the corresponding S_0/S_1 CI and its significance to the Norrish type-I reactions will be discussed in the next Section.

3.4. The S_0/S_1 Conical Intersection

The conical intersection, which plays the role of a "photochemical funnel", is known to be the central mechanistic feature in many nonadiabatic photoreactions.[56–61] Since the process of funneling through a CI is very efficient, the nonradiative decay from the upper to the lower intersecting state usually occurs within a single vibrational period.[60, 61] Furthermore, the structural information of a CI may provide significant insight into the mechanism of photoproduct formation on the ground-state PES.[61, 62, 69, 70]

As illustrated in Figure 17, the bifurcated character of a CI can be represented by a single crossing point of a double cone formed by two intersecting surfaces along the $(n − 2)$-dimensional hyperline, where n is the number of the degrees of freedom in the molecule. The remaining two other coordinates are related to the gradient difference (x_1) and nonadiabatic coupling (x_2) vectors which define a branching space. Accordingly, an S_0/S_1 CI is a structural bottleneck which separates the S_1 state branch of the reaction path from that of S_0. In the direction
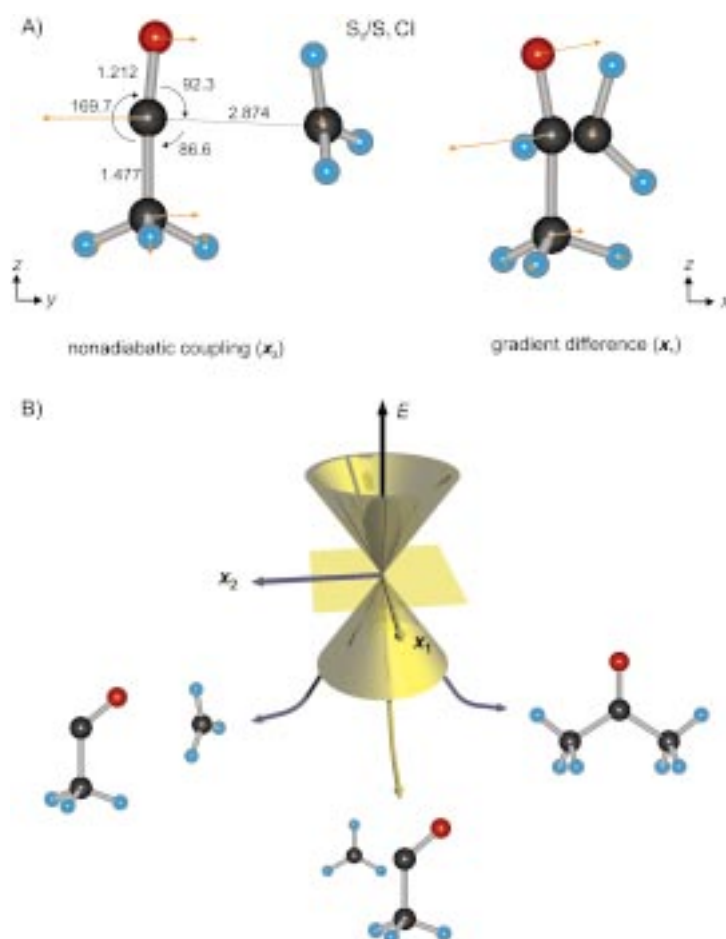

Figure 17. *A) The structure of the S_0/S_1 CI optimized at the CASSCF(10,8)/6-31G(d) level of theory with the corresponding bond lengths [Å] and bond angles [°] as indicated. The nonadiabatic coupling (x_2) and the gradient difference (x_1) vectors are shown with the skeleton of the molecule parallel to the (y, z) and (x, z) plane for the former and the latter, respectively. B) Ground-state branching paths resulting from the S_0/S_1 CI. Following the nonadiabatic coupling vector x_2 either the hot parent molecule (right) or the acyl/alkyl radical pair (left) is produced; following the gradient difference vector x_1 only the acyl/alkyl radical pair is formed.*

of x_1, the difference of the gradients between the S_0 and S_1 surfaces is largest, whereas in the direction of x_2 the electronic and the vibrational coupling of the two states is the best. Moreover, moving from the apex of the conical intersection double cone along this (x_1, x_2) branching space, the energy difference between the S_1 and S_0 states is increased so that the degeneracy of the two states is lifted.

The geometry optimization for the S_0/S_1 CI was carried out by searching for the lowest energy point of the surface crossing seam starting from the last successful point of the reverse IRC path on the S_1 surface of acetone. This was done by minimizing the energy in the $n − 2$ ($= 22$) dimensional intersection space and preserving the degeneracy of the two-dimensional branching space. However, the convergence of the geometry optimization was not improved when the α-CC bond distance increased to ∼2.9 Å and the CCO bond angle approached ∼170°. This lack of improvement primarily results from a very flat potential surface along both the bond-breaking and the methyl-torsion coordinates. To overcome this problem, the

geometry optimization for the S_0/S_1 CI was further performed with the CC bond distance and one of the HCCO dihedral angles fixed. Eventually, the total energy of the S_0/S_1 CI was optimized to be -191.87821 hartree with the S_0/S_1 energy gap less than 10^{-4} hartree. The relative classical energy of the S_0/S_1 CI was calculated to be 25 and 121 kcal mol^{-1} above the S_1 and the S_0 minimum, respectively, at the CASSCF level. However, the total CASSCF energy of the CI is lower than that of the S_1-TS by only 0.00118 hartree (~ 0.7 kcal mol^{-1}). This indicates that the S_1 surface is rather flat along the bond-breaking RC between the S_1-TS and the CI, a feature that is consistent with the convergence problem we have encountered in the geometry optimization for searching the CI.

The optimized structure and the corresponding $\boldsymbol{x}_1$ and $\boldsymbol{x}_2$ vectors are shown in Figure 17 A. Two important points regarding the structure and the two vectors of the S_0/S_1 CI are hereby emphasized. First, the main structural feature of this S_0/S_1 CI is the almost linear CCO bending angle ($169.7°$). This theoretical finding is consistent with the early state-correlation picture of the Salem diagram (Figure 1), which states that the α-cleavage of the S_1 acetone is favored by forming a linear acetyl radical intermediate with topicity value equal to three (tritopic).[3, 5] Furthermore, the linear structural feature of the CCO bending angle in S_0/S_1 CI may imply that the nonradiative dynamics on the S_1 surface are related to the vibrational motions involving substantial changes in the angle. Following the minimum-energy pathway of the S_1 surface, our calculations indicate that the CCO bending angle, while originally $\sim 122°$ in the Franck–Condon region, reduces to $112°$ in the $S_1(C_s)$ minimum geometry. However, the angle expands to $136°$ at the S_1-TS structure and the CCO moiety eventually becomes almost linear at the S_0/S_1 CI region.

Second, the gradient difference and nonadiabatic coupling vectors indicate the possible reaction paths that can be followed on the ground-state surface after the molecule funnels through the CI. As shown in Figure 17 B, the nonadiabatic coupling vector $\boldsymbol{x}_2$ corresponds to a CCO bending motion parallel to the original molecular symmetry plane (y, z), which could lead to formation of either a hot parent molecule or an α-cleavage radical pair. On the other hand, the gradient difference vector $\boldsymbol{x}_1$ corresponds to a CCO bending motion parallel to the (x, z) plane, which could only lead to the radical-pair intermediates. The CI picture indicates that upon excitation to the $S_1(n,\pi^*)$ state of acetone above its S_1 dissociation threshold, it is possible to obtain the bond-dissociation products directly from the S_1 surface via the reaction path overcoming the S_1-TS barrier and then funneling through the S_0/S_1 CI down to the S_0 surface. This feature will be further discussed in the following Section.

3.5. The Two-Dimensional Surfaces and the Minimum-Energy Trajectories

Our previous one-dimensional MEP investigations on the S_1 surface indicate that the CCO bending angle and the α-CC bond length are the two most relevant parameters that can be used to describe the potential energy surface for the Norrish type-I reaction of acetone. To obtain a more extended view of

these two degrees of freedom driving the reaction on the S_1 PES, a two-dimensional surface scan was performed using the TDDFT approach at the B3LYP/6-31G(d) level of theory. Briefly, the resolution of the 2D surface scan was defined with steps of 0.1 Å for the bond length and $10°$ for the bending angle. Then, the single-point energy was calculated starting from the optimized geometry of each species along the bond-breaking RC in the range of $1.1–4.0$ Å and the 2D surface was created by scanning the bending angle in the range of $85–200°$. The 2D contour plot together with the key structures along the minimum-energy pathway of acetone on the S_1 surface are shown in Figure 18.
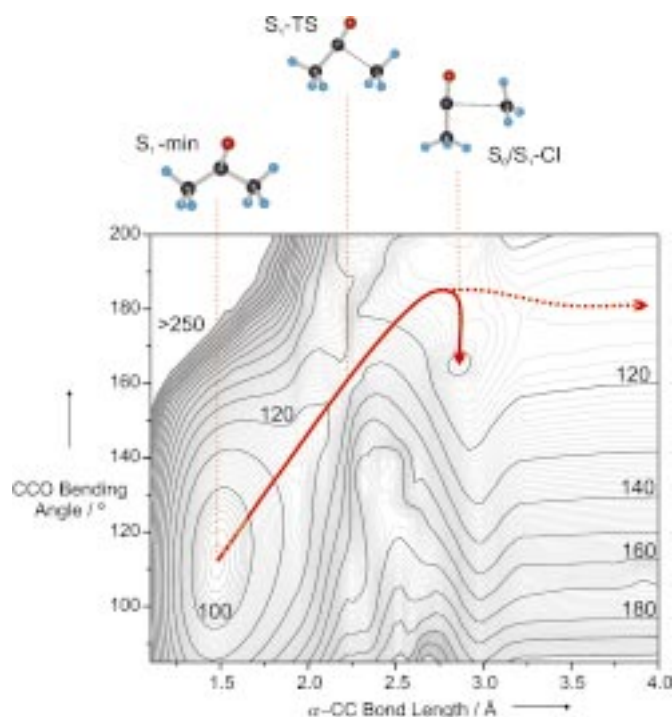

Figure 18. *The contour plot of the S_1 acetone calculated at the TD-UB3LYP/6-31G(d)//CASSCF(10,8)/6-31G(d) level of theory along the CCO bending angle and the α-CC bond-breaking reaction coordinates (see text).*

In order to extract the relevant 2D information from a native multidimensional hypersurface ($n = 24$), the following strategy was applied to scan the surface based on the starting geometry obtained from the MEP along the bond-breaking RC. The S_1 bond-breaking MEP was employed for the bond distances in the range of $1.1–2.1$ Å (Figure 13) and the S_0 bond-breaking MEP was used for the bond distances in the range of $3.0–4.0$ Å (Figure 9). The starting geometry in the intermediate range of the PES ($2.2–2.9$ Å) was obtained from linear interpolation of the structural parameters between the S_1-TS and the S_0/S_1 CI species. Note that the 2D surface was created without geometry relaxation along the bending-angle coordinate, so it may involve a certain amount of uncertainty for the points on the surface far from the bond-breaking MEP region. However, the key feature for the Norrish type-I reaction of acetone taking place on the S_1 PES has been well characterized and demonstrated by the minimum-energy pathways shown as red curves in Figure 18.

The calculated two-dimensional PES has further illuminated several important dynamic features for the α-cleavage of acetone occurring on the $S_1(n,\pi^*)$ surface, that have been discussed in the previous Section. First, in order for the molecule to surmount the lowest energy barrier (S_1-TS) on the S_1 surface, the CCO bending angle of the S_1 species must be substantially increased along the bond-dissociation reaction path. Second, the molecule will reach a relatively flat plateau area with an almost linear CCO configuration after passing over the narrow S_1-TS valley region. Third, there is a funnel clearly shown on the contour plot located at the CCO bending angle of $\sim 165^\circ$ and the CC bond separation of ~ 2.9 Å, which is fully consistent with the S_0/S_1 CI structure optimized at the CASSCF level (Figure 17). Therefore, the excited S_1 acetone molecule can either slightly decrease the CCO bending angle to reach this conical intersection on the S_1 surface (solid arrow trace in Figure 18) or follow the direct dissociation pathway with fixed linear CCO configuration (dotted arrow trace). Note that the latter case would involve overcoming a small additional energy barrier of ~ 2 kcal mol^{-1} according to our calculations.

To further highlight the feature for the S_0/S_1 surface crossing at longer α-CC bond separations, the S_0 and the S_1 2D surfaces are shown in Figure 19 with a 3D perspective view along the CCO bending coordinate. Apparently, both S_0 and S_1 surfaces are approaching each other along the α-CC bond-dissociation pathway as the CCO bending angle is held linear. In the complete bond-dissociation case, the electronic structure of a linear acetyl radical should involve two degenerate configurations, and this feature has been qualitatively demonstrated in Figure 1. The lifting of the degeneracy of the linear acetyl species along the CCO bending coordinate is analogous to the classic example of the Renner–Teller splitting of a linear formyl radical along the HCO bending coordinate due to strong vibronic interactions.[63, 64] Therefore, the trajectory for the α-cleavage of acetone may be represented by the dotted dissociation curve (shown in Figure 18 and 19), which reaches a region where the S_1 surface is in contact with the S_0 surface. From there a bifurcation occurs and leads further to a bent acetyl radical via the CCO bending motion on the S_0 surface (Figure 19). Alternatively, the ground-state bent acetyl radical may also be produced by funneling through the S_0/S_1 CI with the CCO bending motion strongly coupled along the bond-dissociation pathway, which is schematically shown as the solid curve in Figure 19.

3.6. The Ground- and Excited-State Surfaces of Other Ketones

We have also carried out calculations for several model systems using the same CASSCF and the TDDFT approaches in order to generalize the α-cleavage reaction mechanism for the whole family of aliphatic ketones. The purpose of the extended theoretical study is to improve our understanding of how the substituents adjacent to the α-CC bond in a larger ketone affect the α-cleavage process. Therefore, the model systems
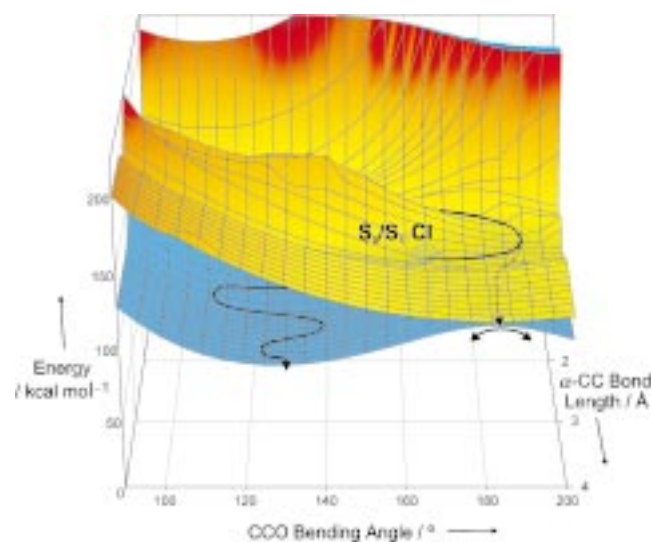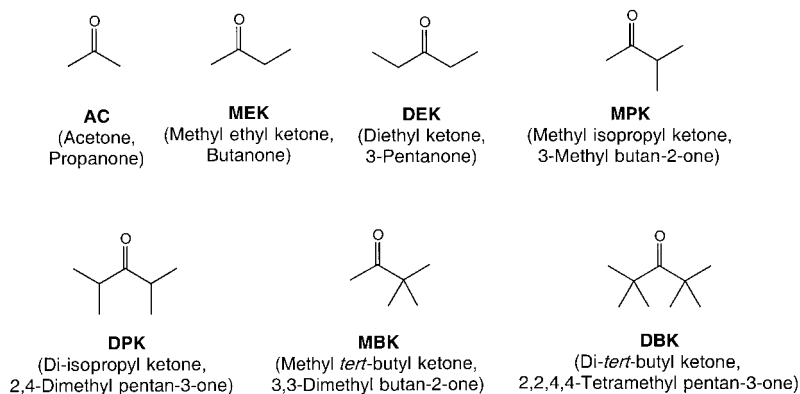

Figure 19. A 3D surface plot for the S_1 and the S_0 PESs of acetone calculated at the TD-UB3LYP/6-31G(d)//CASSCF(10,8)/6-31G(d) level of theory (see text).

basically have the same core structure as acetone, with the difference being the presence of one or more α-methyl substituents (MEK, DEK, MPK, DPK, MBK, and DBK; Scheme 1). The main focus is to calculate the bond-dissociation energy barrier on the S_1 surface for each species and compare it with that of acetone.

The geometries optimized at the CAS(10,8)/6-31G(d) level are shown for the S_0 minima, the S_1 minima, and the corresponding transition states in Figures 20, 21, and 22, respectively. In general, all the geometries of the S_0 minima have a planar OCCC skeleton structure and those of the S_1 minima have the CO group bent out of the CCC symmetry plane. The frequency calculations have confirmed that all the S_0 and S_1 minima have no imaginary frequencies and the S_1 TSs have only one imaginary frequency corresponding to the α-CC bond-dissociation motion. The normal-coordinate vectors with respect to the α-CC bond-breaking RC are shown in Figure 22.

In Table 2 we compare the calculated energies (with ZPE corrections) of each ketone with those of acetone. The relative

AC
(Acetone,
Propanone)

MEK
(Methyl ethyl ketone,
Butanone)

DEK
(Diethyl ketone,
3-Pentanone)

MPK
(Methyl isopropyl ketone,
3-Methyl butan-2-one)

DPK
(Di-isopropyl ketone,
2,4-Dimethyl pentan-3-one)

MBK
(Methyl *tert*-butyl ketone,
3,3-Dimethyl butan-2-one)

DBK
(Di-*tert*-butyl ketone,
2,2,4,4-Tetramethyl pentan-3-one)

Scheme 1. Structures and abbreviated titles of various methyl-substituted acetones.
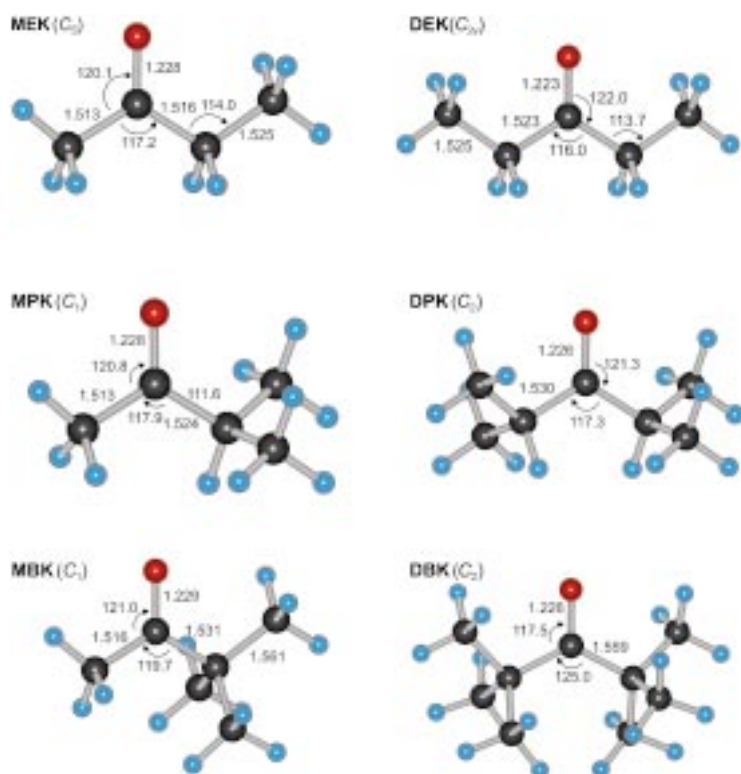
Figure 20. *The structures of the S_0 minimum species for six aliphatic ketones (Scheme 1) optimized at the CASSCF(10,8)/6-31G(d) level of theory with corresponding bond lengths [Å] and bond angles [°] as indicated.*
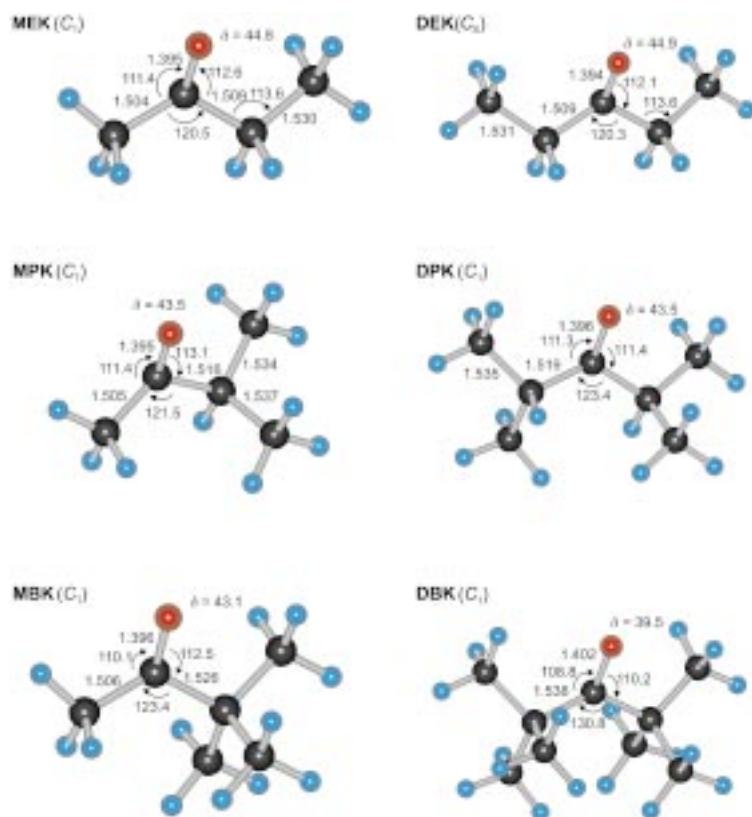

Figure 21. *The structures of the S_1 minimum species for six aliphatic ketones (Scheme 1) optimized at the CASSCF(10,8)/6-31G(d) level of theory with corresponding bond lengths [Å] and bond angles [°] as indicated.*

energies for the S_1 minimum calculated at the CAS(10,8)/6-31G(d) level involve larger uncertainties but they are within the range of 92 – 95 kcal mol^{-1} at the TD-B3P86/6-311 ++ G(d,p) level of theory. On the other hand, the calculated energy barrier for the α-CC bond-breaking process on the S_1 surface indicates an interesting trend for the methyl substitution. For the ketones AC, MEK, MPK, and MBK with common methyl – acyl α-CC bonds, the bond-breaking energy barrier on the S_1 surface can be predicted on average to be 17.9 ± 0.7 (23.0 ± 0.5) kcal mol^{-1} using the TDDFT (CASSCF) method. However, methyl substitution at the α-positions (α-methylations) dramatically reduced the S_1 bond-breaking energy barrier according to our calculations. For symmetrical species like AC, DEK, DPK, and DBK, the S_1 bond-breaking energy barrier is systematically reduced from 18.4 (23.4) kcal mol^{-1} for the methyl – acetyl bond in AC to 12.3 (19.4) kcal mol^{-1} for the ethyl – propionyl bond in DEK, and it is further reduced to 7.4 (17.8) and 7.6 (17.0) kcal mol^{-1} for the isopropyl – isobutanoyl bond in DPK and the *tert*-butyl – pivalyl bond in DBK. Note that α-methylation leads to a significant decrease in the bond-breaking energy barrier for the S_1 ketones predicted at the TDDFT level.[65]

In the case for asymmetrical species, the S_1 bond-breaking energy barrier was calculated to be strongly dependent on different α-methylations. In MEK, the calculated S_1 bond-breaking energy barriers are 16.9 (22.4) and 13.8 (21.5) kcal mol^{-1} for the methyl – propionyl bond and the ethyl – acetyl bond, respectively. But in MPK, they are 17.6 (22.8) and 9.1 (21.2) kcal mol^{-1} for the methyl – isobutanoyl bond and the isopropyl – acetyl bond, respectively; similarly in MBK, they are 18.6 (23.5) and 7.6 (18.3) kcal mol^{-1} for the methyl – pivalyl bond and the *tert*-butyl – acetyl bond, respectively. It is interesting to note that the common methyl – acyl bonds are somehow slightly strengthened upon α-methylation for the asymmetrical S_1 ketones, but the alkyl – acetyl bonds are substantially weakened by α-methylation as in the case for the symmetrical S_1 ketones. These results indicate that the α-CC bond-dissociation process leading to the formation of acetyl and alkyl radicals is the most favorable reaction path upon excitation of an asymmetrical aliphatic ketone to its S_1(n,π*) state. Furthermore, the substantial decrease for the S_1 bond-breaking energy barrier in α-methyl-substituted ketones also suggests that the α-cleavage process in those ketones may subsequently occur in the S_1 state if the excitation energy is sufficient enough to overcome the energy barrier on the S_1 PES. In general, our results indicate that the more the alkyl radical is stabilized by hyperconjugation the lower the S_1 activation energy will be—a finding which is consistent with the Hammond postulate.[66]
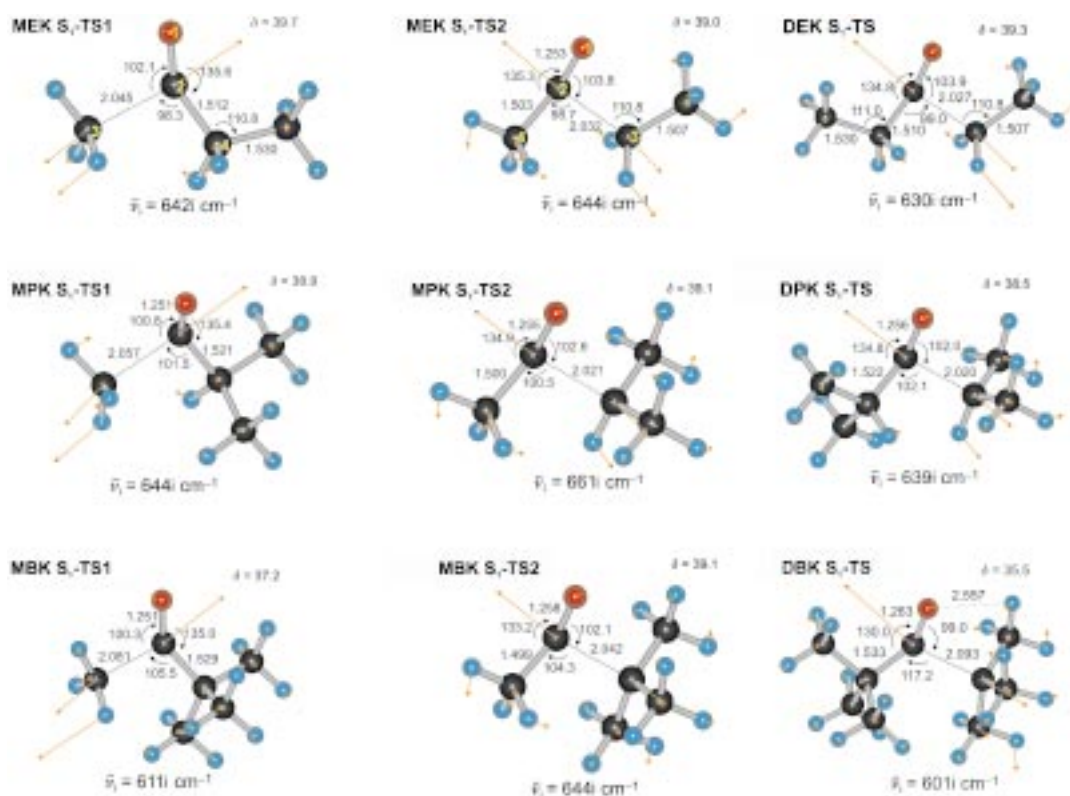
Figure 22. *The structures of the S₁-TS species for six aliphatic ketones (Scheme 1) optimized at the CASSCF(10,8)/6-31G(d) level of theory with corresponding bond lengths [Å] and bond angles [°] as indicated. The vectors represent the normal-coordinate motions of the corresponding imaginary frequencies.*

Table 2. *Total energy E [hartree], $S_1 - S_0$ relative energy ΔE [kcal mol⁻¹], and S_1 energy barrier E_A [kcal mol⁻¹] of various methyl-substituted acetones and cyclic ketones.*

	S₀			S₁					S₁-TS				
	E CAS[a]	ZPE[a,b]	E DFT[c]	E CAS[a]	ZPE[a,b]	E TDDFT[c]	ΔE CAS[a,d]	ΔE DFT[c,d]	E CAS[a]	ZPE[a,b]	E TDDFT[c]	E_A CAS[a,d]	E_A DFT[c,d]
AC	−192.07105	55.9	−193.78815	−191.91855	55.0	−193.63722	94.7	93.7	−191.87703	52.4	−193.60376	23.4	18.4
MEK	−231.08764	74.9	−233.25908	−230.95255	74.3	−233.10723	84.1	94.6	−230.91256	71.6	−233.07599	22.4	16.9
TS2									−230.91472	72.0	−233.08162	21.5	13.8
DEK	−270.14239	94.7	−272.73009	−269.98497	93.6	−272.57719	97.7	94.9	−269.95022	91.2	−272.55378	19.4	12.3
MPK	−270.12095	94.0	−272.72855	−269.98670	93.2	−272.57775	83.5	93.9	−269.94619	90.6	−272.54549	22.8	17.6
TS2									−269.94981	91.3	−272.56004	21.2	9.1
DPK	−348.20977	132.8	−351.66942	−348.05350	131.5	−351.51784	96.8	93.9	−348.01812	129.3	−351.50254	17.8	7.4
MBK	−309.15134	113.1	−312.19774	−309.01963	112.0	−312.04830	81.6	92.7	−308.97784	109.3	−312.01429	23.5	18.6
TS2									−308.98767	110.2	−312.03343	18.3	7.6
DBK	−426.25851	170.8	−430.59887	−426.11086	169.6	−430.45055	91.4	91.8	−426.08027	167.4	−430.43489	17.0	7.6
CB[e]	−229.86830	60.7	−231.97901	−229.75501	60.3	−231.82710	73.7	94.8	−229.73865	58.5	−231.82501	5.4	< 1.0[f]
CP[e]	−268.95507	81.3	−271.48033	−268.81651	80.3	−271.33120	86.0	92.6	−268.78742	78.3	−271.31061	16.3	10.9

[a] CASSCF(10,8)/6-31G(d). [b] Zero-point energy [kcal mol⁻¹]. [c] B3P86/6-311 + + G(d,p)//CASSCF(10,8)/6-31G. [d] With ZPE corrections. [e] Two cyclic ketone examples for comparison: cyclobutanone CB and cyclopentanone CP; see ref. [38] for details. [f] The energy barrier of CB disappears after ZPE correction.[38]

3.7. A General Norrish type-I Reaction Mechanism

First we consider the measured fluorescence lifetime as a function of excess internal energy above the S₁ origin for acetone. The observed microsecond fluorescence decay lifetimes near the 0-0 origin ($\lambda_{ex} = 328.6$ nm) was proposed to be due to the S₁ →S₀ IC process because of the relatively efficient vibronic coupling between the S₁ and the S₀ states.[34] Note that

the radiative lifetime of acetone for the S₁ →S₀ fluorescence was predicted to be ∼ 10 μs.[29, 34c] Above the excess internal energy of ∼ 900 cm⁻¹ ($\lambda_{ex} \sim 320$ nm), the S₁ →T₁ ISC process was additionally observed in the fluorescence signal.[34] The measured fluorescence lifetime decreases abruptly at the excess energy of ∼ 2250 cm⁻¹ ($\lambda_{ex} \sim 306$ nm), which provided evidence for the bond dissociation on the triplet surface.[34d] Our calculations indicate that the energy of the T₁ surface is very close to that of

the S_1 surface (Table 1), thus the $S_1 \rightarrow T_1$ ISC process should be a very efficient route for the excited molecule to relax from its $S_1(n,\pi^*)$ excited state.[29, 67] In fact, there is an S_1/T_1 surface crossing point located above the S_1 minimum by ~ 18 kcal mol^{-1} predicted at the CAS(8,7)/6-31G(d) level of theory.[11]

The energy barrier along the α-CC bond-breaking RC on the T_1 surface was calculated to be ~ 90 kcal mol^{-1} above the S_0 minimum, which is consistent with the observation of a sudden change in fluorescence lifetime at the threshold of 91.5 or 93.5 kcal mol^{-1}.[13, 34d] For the excitation energy above the T_1 dissociation threshold, the S_1 lifetime was reported to smoothly decrease from 2.1 ns at $\lambda_{ex} \sim 295$ nm down to < 1.6 ns at $\lambda_{ex} \sim 260$ nm.[33] Our study indicates that the direct bond dissociation of an S_1 acetone requires the molecule to overcome an energy barrier of ~ 20 kcal mol^{-1} along the bond-breaking RC on the S_1 surface. Therefore, it is possible for the direct S_1 bond-dissociation channel of acetone to compete with the ISC process if sufficient excitation energy can be provided.

According to our theoretical and experimental findings and previous spectroscopic evidence, a mechanism is presented in Scheme 2 to rationalize the observed photochemical behavior of
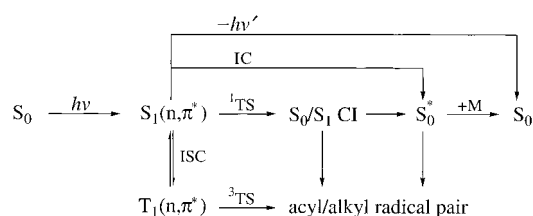
Scheme 2. Photochemistry of aliphatic ketones upon excitation to the S_1 state.

acetone and other aliphatic ketones upon excitation to the S_1 state. It is believed that the traditionally accepted $S_1 \rightarrow T_1$ ISC process should be the dominant channel when the excitation energy is lower than the S_1 bond-dissociation threshold. However, when the excitation energy is higher than the S_1 dissociation threshold, one should also consider the reaction path via the direct S_1 bond-dissociation channel to form the acyl/alkyl radical pair through the S_0/S_1 CI. Such a direct S_1 bond-dissociation pathway may become increasingly important as the S_1 energy barrier is reduced, in particular for those aliphatic ketones involving isopropyl or *tert*-butyl group(s), as summarized in Table 2.

We would like to address once more—from the theoretical point of view—the conclusion made by recent femtosecond mass spectroscopic studies.[24, 26] The question is the following: Given an excitation energy slightly above or close to the S_1 bond-breaking threshold (110 kcal mol^{-1} or 260 nm), will the primary α-CC bond of acetone break in less than 200 fs (that is, promptly)?

According to the theoretical evidence we have discussed above, the prompt α-cleavage mechanism on the S_1 surface faces two problems: a) Transferring the excess internal energy from the originally activated vibrational modes (b_1 out-of-plane CO bending motion) to the bond-breaking RC (b_2 asymmetrical in-plane CC stretch) and overcoming an energy barrier as high as 20 kcal mol^{-1} should take much longer than 200 fs. b) Alternatively, an efficient $S_1 \rightarrow T_1$ ISC process followed by a rapid bond dissociation on the T_1 surface is very unlikely to take place in less than 200 fs. Therefore, the α-cleavage of acetone on the S_1 PES should occur on a much longer time scale (nanoseconds), in accord with early fluorescence measurements,[29, 33] and the fs dynamics is that of the early motion from the FC region.

3.8. A Physical Picture Based on Valence-Bond Theory

In the following, we discuss the α-cleavage process of acetone occurring on the S_0, S_1, and T_1 surfaces using a simple atomic-orbital (AO) model within the framework of valence-bond (VB) theory. A simple physical picture is shown in Figures 23 and 24, with the six relevant valence electrons (two carbonyl π-electrons, one pair of oxygen nonbonding electrons, and the two σ-electrons of the α-CC bond) primarily involved in the α-cleavage processes. In our model, we describe the hybridization of the AOs in the carbonyl group of the ground-state acetone molecule ($\tilde{X}^1A_1$) to have sp^2 hybrids on the carbon atom but sp hybrids on the oxygen atom. The n $\rightarrow\pi^*$ electronic transition places acetone on the S_1 surface with FC configuration ($\tilde{A}^1A_2$), which is
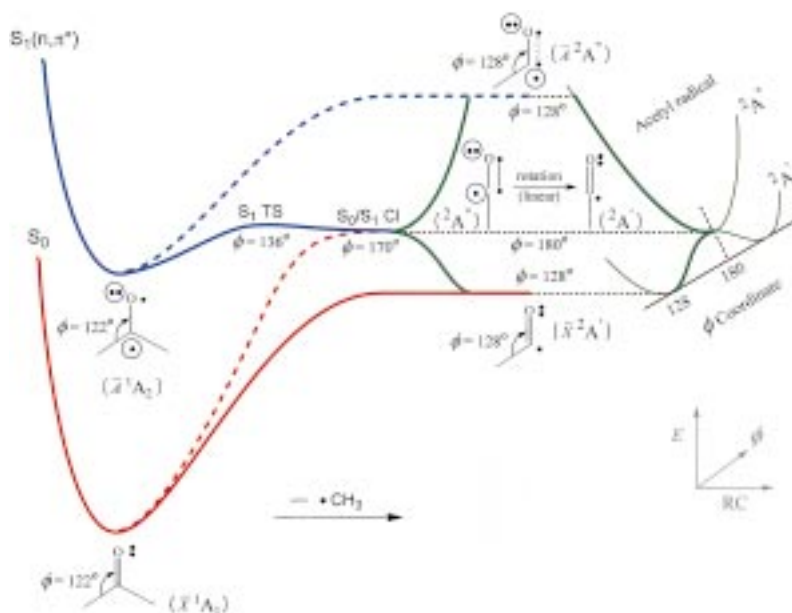
Figure 23. The α-cleavage reaction coordinate diagram of acetone along the S_0 and S_1 MEPs representing the most favorable reaction pathways for the thermal (red solid curve) and the photochemical (blue solid curve) processes, respectively; the corresponding S_1 and S_0 potential energy curves are shown as blue and red broken lines, respectively. The green tilted lines on the right side indicate two corresponding potential energy curves of acetyl radical along its CCO bending coordinate (ϕ) when the first α-CC bond of acetone is completely cleaved. The electronic structures of each species are drawn according to a simple valence-bond model (see text).
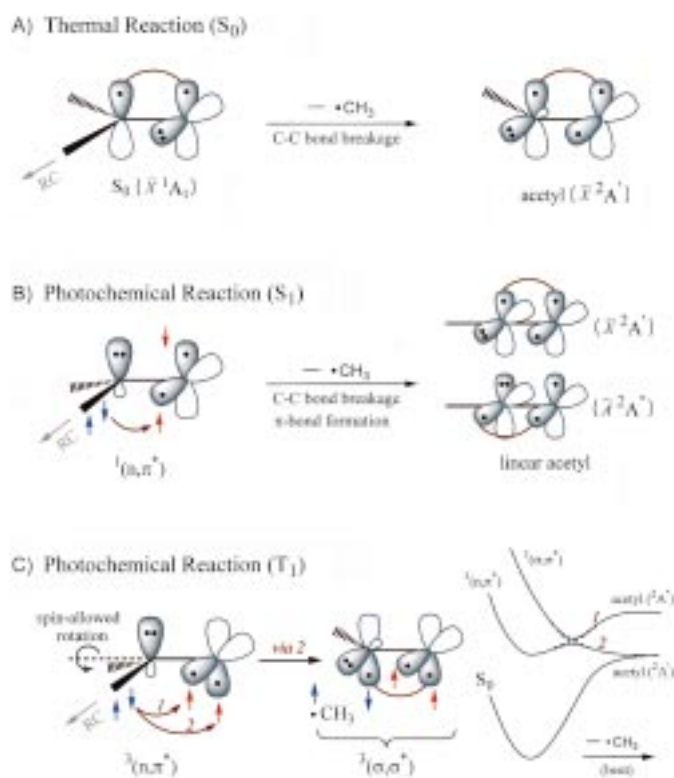
Figure 24. *A schematic orbital picture representing the α-cleavage of acetone via A) the thermal reaction path, B) the photochemical process on the S_1 surface, and C) the process on the T_1 surface. The processes involve bond breakage with the same sp^2 hybridization of the carbon atom (A), bond formation and breakage with bending-type rehybridization to a sp carbon atom (B), or bond formation and breakage with rotation-type rehybridization to a sp^2 carbon atom (C). The detailed discussion is given in the text.*

involve a simple α-CC bond-breaking process to asymptotically produce the corresponding radical pair at different electronic states. Accordingly, the photochemical process along the bent reaction path is highly unfavorable (see also Figure 1). However, rehybridization of three sp^2 orbitals of the central carbon atom into one p and two sp orbitals is an energetically favorable process to effectively make a new π-bond between the two in-plane p orbitals of the carbonyl group. Note that the process of rehybridization requires the geometry of the CCO moiety to become *linear*, which is a key feature for the photochemical α-cleavage process to occur on the S_1 surface. The difference between the thermal and the photochemical reactions can be understood as follows: The thermal process involves only simple CC bond breakage, while the photochemical process involves not only the CC bond breakage but also the π-bond formation via rehybridization of the sp^2 orbitals into sp and p orbitals. This concept is schematically illustrated in Figure 24.

Our final remarks concern the energy barrier for the photochemical process of the α-cleavage of acetone occurring on the S_1 and T_1 surfaces. According to the above discussion, the fundamental discrepancy between the equilibrium ground-state acetyl ($\tilde{X}^2A'$) and the bent excited-state acetyl ($\tilde{A}^2A''$) is the location of the unpaired electron with respect to the molecular symmetry plane—for the former it is in-plane but for the latter it is perpendicular to the molecular plane (Figure 23). In other words, to make a "stable" ground-state acetyl radical from a photochemical process, the new carbonyl π-bond must be reformed in a configuration that is perpendicular to the molecular symmetry plane. Figures 24 B and 24 C show the simple picture for how the Norrish type-I reaction of acetone overcomes the corresponding energy barriers along the S_1 and T_1 surfaces, respectively. This simple VB picture shows that a direct rehybridization of the carbon atom to sp^2 orbitals in a rotation-type manner along the α-cleavage RC on the S_1 surface is not applicable (Figure 24 B). Thus, the Norrish type-I reaction on the S_1 surface is expected to occur through the bending-type rehybridization that leads to the acetyl moiety with a *linear* configuration, as we have discussed before.

However, this rotation-type rehybridization on the T_1 surface is allowed so that a new CO π-bond perpendicular to the molecular symmetry plane can be formed via process *2*, as indicated in Figure 24 C. Note that process *1* describes the triplet α-cleavage to bent-acetyl geometry, which is analogous to its singlet counterpart shown as blue broken curve in Figure 23. Process *2* characterizes the triplet α-cleavage process along the $^3(σ,σ^*)$ surface at longer CC bond distances; a repulsive potential curve is anticipated if one follows the reverse path of process *2* along the $^3(σ,σ^*)$ surface at shorter CC bond distances (Figure 24 C). Therefore, the existence of a small barrier for α-cleavage on the T_1 surface is the result of an avoided crossing between two surfaces corresponding to the $^3(n,π^*)$ "forbidden" dissociation (leading to the excited-state A'' acetyl) and the $^3(σ,σ^*)$ repulsive processes (giving the ground-state A' acetyl).[6, 9] This qualitative VB picture is entirely consistent with our high-level ab initio (MO)/DFT calculations that the energy barrier on the T_1 surface is much lower than the barrier on the S_1 surface (Table 1).

characterized by three π-electrons (circled in Figure 23) inside the two p orbitals perpendicular to the molecular plane.

The thermal (S_0) and photochemical (S_1) MEPs are indicated in Figure 23 as red and blue solid curves, respectively; the corresponding S_0 and S_1 PESs are shown as broken curves. According to our calculations, the CCO bending angle changes only slightly (from $\phi = 122°$ to $\phi = 128°$) along the thermal reaction path on the S_0 surface (Figure 9), whereas this angle increases enormously (from the FC structure changing to the almost linear configuration) along the photochemical reaction path on the S_1 surface (Figures 13 and 18). Therefore, in theory the thermal reaction (Figure 24 A) directly gives a bent ground-state acetyl ($\tilde{X}^2A'$), whereas the photochemical reaction on the S_1 surface (Figure 24 B) would at first lead to a linear acetyl at which configuration both electronic states ($\tilde{X}^2A'$ and $\tilde{A}^2A''$) are degenerate (Figure 23).

The blue broken curve shows the α-cleavage process on the S_1 surface along the bent reaction path (S_0 MEP), which produces a bent acetyl at the first excited state ($\tilde{A}^2A''$). The dotted line connecting the two electrons in the bent acetyl ($\tilde{A}^2A''$) represents the incomplete π-bond "formed" between a p and an sp^2 orbital. Therefore, it is not surprising that both the blue broken (photochemical) and the red solid (thermal) potential energy curves shown in Figure 23 are similar in shape—they both

4. Conclusion

Based on our experimental and theoretical findings, a general picture for the observed S_1 dynamics of acetone on the global multidimensional potential energy surfaces has been deduced and is summarized as follows.

a) Upon excitation by a femtosecond laser pulse at $\lambda_{ex} = 307$ nm, the molecule is promoted to the S_1 surface. The initial dephasing out of the Franck–Condon region on the $S_1(n,\pi^*)$ state was observed to occur in less than 50 fs.

b) The driving forces for the nuclear motions of acetone upon excitation to the $S_1(n,\pi^*)$ state are perpendicular transitions corresponding to the mixed CO stretching/CO out-of-plane bending and the CH_3 torsional motions (Figure 8).

c) Following the minimum-energy α-cleavage reaction path over the energy barrier on the S_1 surface down to the S_0 surface, the structural changes at each stationary point along the pathway are substantial. In particular, the CCO bending angle changes considerably: $122°$ at the S_1 Franck–Condon region to $112°$ at the S_1 minimum, increasing to $136°$ at the S_1 transition state, and becoming $170°$ when reaching the S_0/S_1 CI region. Funneling through the conical intersection to the ground-state surface leads to either the α-cleavage radical pair or a hot parent molecule (Figure 17).

d) The S_1 energy barrier of acetone along the α-CC bond-breaking RC to reach the S_0/S_1 CI was calculated to be 18 kcal mol^{-1} ($\sim$110 kcal mol^{-1} above the S_0 minimum). However, the α-CC bond-dissociation energy barrier on the T_1 surface was calculated to be only $\sim$90 kcal mol^{-1} above the S_0 minimum, in accordance with the experimental dissociation threshold observed by Copeland and Crosley[13] and Haas and co-workers.[34]

e) Based on a simple atomic-orbital model within the framework of VB theory, the α-cleavage on the S_1 surface can be understood to involve the rehybridization of the sp^2 orbitals into the sp and p orbitals through a linear CCO configuration in order for the two in-plane p orbitals to form a new π-bond while breaking the α-CC bond along the RC (Figure 23). On the other hand, the α-cleavage on the T_1 surface is spin-allowed for the rotation-type rehybridization to make a new CO π-bond perpendicular to the molecular plane along the RC. The idea for "rotation" of the orbitals about the CO bond in a way is similar to the concept of finding a lowest avoided crossing point between the $^3(n,\pi^*)$ and the $^3(\sigma,\sigma^*)$ surfaces along the triplet α-cleavage RC. However, such a rotation (or avoided crossing) on the S_1 surface is strictly spin-forbidden (Figure 24), which may provide a theoretical foundation to explain why the energy barrier on the S_1 surface is much higher than the barrier on the T_1 surface along the α-cleavage RC.

f) Since the available energy due to one-photon excitation is 93 kcal mol^{-1}, which is below the S_1 barrier but above the T_1 barrier for the α-CC bond dissociation, the observed slow build-up signal is assigned to be the formation of the acetyl radical after the rate-limiting $S_1 \rightarrow T_1$ ISC process. This direct observation is consistent with early fluorescence results[29, 33] showing the S_1 lifetime of acetone to be on the ns time scale

but contradicts the more recent conclusion that the S_1 α-cleavage is prompt.

g) The S_1 α-cleavage barrier in other aliphatic ketones was calculated to be substantially lower than that of acetone by methyl substitutions at the α-position (Table 2). Therefore, the direct S_1 bond-dissociation channel for those aliphatic ketones should also be considered if sufficient internal energy is available.

h) A general picture for the Norrish type-I reaction mechanism of an aliphatic ketone upon excitation to the $S_1(n,\pi^*)$ state is schematically demonstrated in Figure 25.
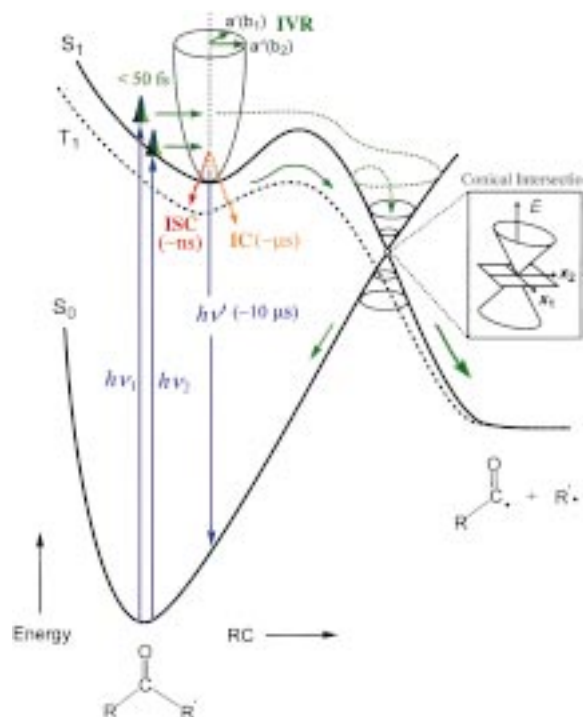

Figure 25. *A schematic reaction coordinate (RC) diagram along the α-cleavage RC of a ketone molecule showing an overview of the proposed photochemical reaction mechanism and the related time scales of each processes. The wave packet is prepared in two ways: Excitation by $h\nu_1$ prepares the packet above the S_1 bond-dissociation threshold whereas excitation by $h\nu_2$ prepares the packet below the S_1 threshold and, in both cases, the packet rapidly propagates to the S_1 local minimum region. The multidimensional feature of the S_1 surface is represented by a semi-ellipsoid column with the arrows representing the direction of the vibrational motions: The $a''(b_2)$ normal modes are parallel to the α-bond-breaking RC while the $a'(b_1)$ modes are perpendicular to the RC. The wavy curves represent two major nonradiative relaxation processes below the S_1 threshold—the $S_1 \rightarrow T_1$ intersystem crossing (ISC) and the $S_1 \rightarrow S_0$ internal conversion (IC). The trajectory (dotted arrow) shows a typical α-cleavage reaction path above the bond-dissociation threshold on the S_1 surface going down to search for the S_0/S_1 conical intersection and eventually leading to the ground-state product channels.*

[1] W. A. Noyes, Jr. in *Photochemistry and Reaction Kinetics* (Eds.: P. G. Ashmore, F. S. Dainton, T. M. Sugden), Cambridge University Press, Cambridge, **1967**, pp. 1 – 25.

[2] J. Michl, V. Bonaic-Koutecky, *Electronic Aspects of Organic Photochemistry*, Wiley, New York, NY, **1990**.

[3] N. J. Turro, *Modern Molecular Photochemistry*, University Science Books, Sausalito, CA, **1991**.

[4] J. Kopecky, *Organic Photochemistry: A Visual Approach*, VCH, New York, NY, **1992**.

[5] M. Klessinger, J. Michl, *Excited States and Photochemistry of Organic Molecules*, VCH, New York, NY, **1995**.

[6] L. Salem, *J. Am. Chem. Soc.* **1974**, *96*, 3486 – 3501, and references therein.

[7] M. Reinsch, M. Klessinger, *J. Phys. Org. Chem.* **1990**, *3*, 81 – 88.

[8] a) O. Setokuchi, Y. Simizu, *J. Mol. Struct. (Theochem)* **1997**, *401*, 29 – 33; b) O. Setokuchi, S. Matuzawa, Y. Shimizu, *Chem. Phys. Lett.* **1998**, *284*, 19 – 23.

[9] H. Sakurai, S. Kato, *J. Mol. Struct. (Theochem)* **1999**, *461*, 145 – 152.

[10] X. Li, Z. Li, S. Ma, *Sci. China Ser. B* **1999**, *42*, 373 – 381.

[11] D. Liu, W. Fang, X. Fu, *Chem. Phys. Lett.* **2000**, *325*, 86 – 92.

[12] E. K. C. Lee, R. S. Lewis, *Adv. Photochem.* **1980**, *12*, 1 – 95, and references therein.

[13] R. A. Copeland, D. R. Crosley, *Chem. Phys. Lett.* **1985**, *115*, 362 – 368.

[14] a) D. J. Donaldson, S. R. Leone, *J. Chem. Phys.* **1986**, *85*, 817 – 824; b) E. L. Woodbridge, T. R. Fletcher, S. R. Leone, *J. Phys. Chem.* **1988**, *92*, 5387 – 5393.

[15] P. D. Lightfoot, S. P. Kirwan, M. J. Pilling, *J. Phys. Chem.* **1988**, *92*, 4938 – 4946.

[16] K. A. Trentelman, S. H. Kable, D. B. Moss, P. L. Houston, *J. Chem. Phys.* **1989**, *91*, 7498 – 7513.

[17] Y. Haas, *Spectrochim. Acta Part A* **1990**, *46*, 541 – 549, and references therein.

[18] G. E. Hall, V. Bout, T. J. Sears, *J. Chem. Phys.* **1991**, *94*, 4182 – 4188.

[19] L. D. Waits, R. J. Horwitz, J. A. Guest, *Chem. Phys.* **1991**, *155*, 149 – 156.

[20] S. W. North, D. A. Blank, J. D. Gezelter, C. A. Longfellow, Y. T. Lee, *J. Chem. Phys.* **1995**, *102*, 4447 – 4460.

[21] S. K. Kim, S. Pedersen, A. H. Zewail, *J. Chem. Phys.* **1995**, *103*, 477 – 480.

[22] T. Shibata, T. Suzuki, *Chem. Phys. Lett.* **1996**, *262*, 115 – 119.

[23] C. Maul, K. Gericke, *Int. Rev. Phys. Chem.* **1997**, *16*, 1 – 79, and references regarding the three-body photodissociation topics therein.

[24] a) S. A. Buzza, E. M. Snyder, A. W. Castleman, Jr., *J. Chem. Phys.* **1996**, *104*, 5040 – 5047; b) S. A. Buzza, E. M. Snyder, D. A. Card, D. E. Folmer, A. W. Castleman, Jr., *J. Chem. Phys.* **1996**, *105*, 7425 – 7431; c) Q. Zhong, L. Poth, A. W. Castleman, Jr., *J. Chem. Phys.* **1999**, *110*, 192 – 196.

[25] C. Majumder, O. D. Jayakumar, R. K. Vatsa, S. K. Kulshreshtha, J. P. Mittal, *Chem. Phys. Lett.* **1999**, *304*, 51 – 59.

[26] a) J. C. Owrutsky, A. P. Baronavski, *J. Chem. Phys.* **1998**, *108*, 6652 – 6659; b) J. C. Owrutsky, A. P. Baronavski, *J. Chem. Phys.* **1999**, *110*, 11 206 – 11 213.

[27] P. Farmanara, V. Stert, W. Radloff, *Chem. Phys. Lett.* **2000**, *320*, 697 – 702.

[28] M. Emrich, P. Warneck, *J. Phys. Chem. A* **2000**, *104*, 9436 – 9442.

[29] D. A. Hansen, E. K. C. Lee, *J. Chem. Phys.* **1975**, *62*, 183 – 189.

[30] P. R. Bunker, P. Jensen, *Molecular Symmetry and Spectroscopy*, 2nd ed., NRC Research Press, Ottawa, ON, **1998**, pp. 435 – 439.

[31] D. W. Liao, A. M. Mebel, M. Hayashi, Y. J. Shiu, Y. T. Chen, S. H. Lin, *J. Chem. Phys.* **1999**, *111*, 205 – 215.

[32] a) M. Baba, I. Hanazaki, *Chem. Phys. Lett.* **1983**, *103*, 93 – 97; b) M. Baba, I. Hanazaki, U. Nagashima, *J. Chem. Phys.* **1985**, *82*, 3938 – 3947.

[33] G. M. Breuer, E. K. C. Lee, *J. Phys. Chem.* **1971**, *75*, 989 – 990.

[34] a) O. Anner, H. Zuckermann, Y. Haas, *J. Phys. Chem.* **1985**, *89*, 1336 – 1339; b) H. Zuckermann, B. Schmits, Y. Haas, *J. Phys. Chem.* **1988**, *92*, 4835 – 4837; c) H. Zuckermann, B. Schmits, Y. Haas, *Chem. Phys. Lett.* **1988**, *151*, 323 – 327; d) H. Zuckermann, B. Schmits, Y. Haas, *J. Phys. Chem.* **1989**, *93*, 4083 – 4091.

[35] J. Heicklen, *J. Am. Chem. Soc.* **1959**, *81*, 3863 – 3866.

[36] G. Hancock, K. R. Wilson, in *Proc. Fourth Int. Symp. Molecular Beams* (Cannes, France) **1973**, pp. 511 – 533.

[37] N. J. Turro, W. E. Farenth, A. Devaquet, *J. Am. Chem. Soc.* **1976**, *98*, 7425 – 7427.

[38] E. W.-G. Diau, C. Kötting, A. H. Zewail, *ChemPhysChem*, **2001**, *2*, 294 – 309, the following paper in this issue.

[39] The S_1 lifetime of acetone τ_S at $\lambda_{ex} = 307$ nm was estimated to be ~ 2.5 ns and ~ 3.0 ns for [D_0]- and [D_6]acetone, respectively, based on the results of Lee and co-workers.[29, 33]

[40] The kinetic isotope effect of acetone at our wavelength of interest (307 nm) is not substantial [$\tau([D_0]AC)^{-1}/\tau([D_6]AC)^{-1} \sim 1.2$] and it is not obviously seen in the plot (Figure 4 A) due to the limitation of the pump – probe delay times of the transients.

[41] Our excited-state calculations (TDDFT) indicate that the energy required for a vertical electronic transition from the S_1 to the S_2 state (at the S_1 minimum geometry) and from the ground state of the acetyl radical to its first excited state is 3.1 and 2.4 eV, respectively. Using the probe pulse of 2 eV ($\lambda_{probe} = 615$ nm) in our experiments, it is expected to establish the resonance-enhanced condition for the MPI signal of a cold acetyl radical at the CCO bending angle slightly larger than the angle at the equilibrium geometry (see also Figure 23).

[42] J. D. Goddard, G. Orlova, *J. Chem. Phys.* **1999**, *111*, 7705 – 7712.

[43] M. Merchan, B. O. Roos, R. McDiardmid, X. Xing, *J. Chem. Phys.* **1996**, *104*, 1791 – 1804.

[44] A. D. Becke, *J. Chem. Phys.* **1993**, *98*, 5648 – 5652.

[45] C. Lee, W. Yang, R. G. Parr, *Phys. Rev. B* **1988**, *37*, 785.

[46] W. Hehre, L. Radom, P. von R. Schleyer, J. A. Pople, *Ab Initio Molecular Orbital Theory*, Wiley, New York, NY, **1986**.

[47] F. Jensen, *Introduction to Computational Quantum Chemistry*, Wiley, New York, NY, **1998**.

[48] K. B. Wiberg, R. E. Stratmann, M. J. Frisch, *Chem. Phys. Lett.* **1998**, *297*, 60 – 64.

[49] D. J. Tozer, N. C. Handy, *Phys. Chem. Chem. Phys.* **2000**, *2*, 2117 – 2121.

[50] a) P. Brint, L. O'Toole, S. Couris, D. Jardine, *J. Chem. Soc. Faraday Trans.* **1991**, *87*, 2891 – 2895; b) L. O'Toole, P. Brint, C. Kosmidis, G. Boulakis, P. Tsekeris, *J. Chem. Soc. Faraday Trans.* **1991**, *87*, 3343 – 3351.

[51] *Gaussian 98* (Rev. A.9), M. J. Frisch, G. W. Trucks, H. B. Schlegel, G. E. Scuseria, M. A. Robb, J. R. Cheeseman, V. G. Zakrzewski, J. A. Montgomery, R. E. Stratmann, J. C. Burant, S. Dapprich, J. M. Millam, A. D. Daniels, K. N. Kudin, M. C. Strain, O. Farkas, J. Tomasi, V. Barone, M. Cossi, R. Cammi, B. Mennucci, C. Pomelli, C. Adamo, S. Clifford, J. Ochterski, G. A. Petersson, P. Y. Ayala, Q. Cui, K. Morokuma, D. K. Malick, A. D. Rabuck, K. Raghavachari, J. B. Foresman, J. Cioslowski, J. V. Ortiz, B. B. Stefanov, G. Liu, A. Liashenko, P. Piskorz, I. Komaromi, R. Gomperts, R. L. Martin, D. J. Fox, T. Keith, M. A. Al-Laham, C. Y. Peng, A. Nanayakkara, C. Gonzalez, M. Challacombe, P. M. W. Gill, B. G. Johnson, W. Chen, M. W. Wong, J. L. Andres, M. Head-Gordon, E. S. Replogle, J. A. Pople, Gaussian, Inc., Pittsburgh, PA, **1998**.

[52] See, for example, E. W.-G. Diau, S. C. Smith, *J. Phys. Chem.* **1996**, *100*, 12 349 – 12 354.

[53] T. Baer, W. L. Hase, *Unimolecular Reaction Dynamics*, Oxford University Press, New York, NY, **1996**.

[54] The local minimum was found located at RC = 4.240 and 3.784 Å based on the CASSCF and the DFT calculations, respectively. The spurious point (local minimum) located in the middle of the MEP may be due to the following reason: The long-range dipole – dipole interaction becomes predominant over the short-range CC valence-bond interaction at longer separations leading to a van der Waals complex as an intermediate along the RC. Therefore, at RC > 4 Å, the single α-CC bond-breaking MEP is characterized mainly by the stronger long-range interaction between the hydrogen atom of the departing methyl group and the radical center of the acetyl group. This feature is best demonstrated by the drastic change of the geometry along the MEP near the local minimum region, where the departing methyl group suddenly flips to have a nearly linear CHC configuration. This is also the reason why the θ angle predicted at the UB3LYP/6-31G(d) level suffered a dramatic variation in the RC range between 3.8 and 4.2 Å, as shown in Figure 9 A.

[55] a) N. N. Yakovlev, I. V. Dyumaeva, I. A. Godunov, *Russ. J. Phys. Chem.* **1992**, *66*, 367 – 371; b) N. N. Yakovlev, I. A. Godunov, *Russ. J. Phys. Chem.* **1995**, *69*, 507 – 510.

[56] I. N. Ragazos, M. A. Robb, F. Bernardi, M. Olivucci, *Chem. Phys. Lett.* **1992**, *197*, 217 – 223.

[57] W. Domcke, G. Stock, *Adv. Chem. Phys.* **1997**, *100*, 1.

[58] D. R. Yarkony, *Acc. Chem. Res.* **1998**, *31*, 511 – 518.

[59] M. Klessinger, *Angew. Chem.* **1995**, *107*, 597 – 599; *Angew. Chem. Int. Ed. Engl.* **1995**, *34*, 549 – 551.

[60] F. Bernardi, M. Olivucci, M. A. Robb, *Chem. Soc. Rev.* **1996**, *25*, 321 – 328, and references therein.

[61] S. Wilsey, K. N. Houk, A. H. Zewail, *J. Am. Chem. Soc.* **1999**, *121*, 5772 – 5786, and references therein.

[62] a) E. W.-G. Diau, O. K. Abou-Zied, A. A. Scala, A. H. Zewail, *J. Am. Chem. Soc.* **1998**, *120*, 3245 – 3246; b) E. W.-G. Diau, S. De Feyter, A. H. Zewail, *Chem. Phys. Lett.* **1999**, *304*, 134 – 144; c) S. De Feyter, E. W.-G. Diau, A. H. Zewail, *Phys. Chem. Chem. Phys.* **2000**, *2*, 877 – 883.

[63] G. Herzberg, *Molecular Spectra and Molecular Structure, III. Electronic Spectra and Electronic Structures of Polyatomic Molecules*, Van Nostrand, New York, NY, **1966**.

[64] A. Loettgers, A. Untch, H. Keller, R. Schinke, H. Werner, C. Bauer, P. Rosmus, *J. Chem. Phys.* **1997**, *106*, 3186 – 3204, and references therein.

[65] The even more dramatic change of the S_1 α-cleavage energy barrier has been predicted for cyclic ketones (Table 2), which is due to not only the α-methylation but also the additional ring-strain effect. Particularly in the four-membered cyclic ketone, cyclobutanone (CB in Table 2), the observed anomalous nonradiative dynamics on the S_1 surface will be discussed and detailed in our subsequent paper.[38]

[66] G. S. Hammond, *J. Am. Chem. Soc.* **1955**, *77*, 334 – 338.

[67] N. C. Yang, E. D. Feit, M. H. Hui, N. J. Turro, J. C. Dalton, *J. Am. Chem. Soc.* **1970**, *92*, 6974 – 6976.

[68] A. H. Zewail, *Femtochemistry: Ultrafast Dynamics of the Chemical Bond*, *Vol. I and II*, World Scientific, Singapore, **1994**, and references therein.

[69] E. W.-G. Diau, S. De Feyter, A. H. Zewail, *J. Chem. Phys.* **1999**, *110*, 9785 – 9788.

[70] D. Zhong, E. W.-G. Diau, T. M. Bernhardt, S. De Feyter, J. D. Roberts, A. H. Zewail, *Chem. Phys. Lett.* **1998**, *298*, 129 – 140.